

Evolution of skewness and kurtosis of cosmic density fields

Jaana Einasto^{1,2,3}, Anatoly Klypin⁴, Gert Hütsi⁵, Lauri-Juhan Liivamägi¹, and Maret Einasto¹

¹ Tartu Observatory, University of Tartu, EE-61602 Tõravere, Estonia

² ICRANet, Piazza della Repubblica 10, 65122 Pescara, Italy

³ Estonian Academy of Sciences, 10130 Tallinn, Estonia

⁴ Astronomy Department, New Mexico State University, Las Cruces, NM 88003, USA

⁵ National Institute of Chemical Physics and Biophysics, Tallinn 10143, Estonia

Received; accepted

ABSTRACT

Aims. We investigate the evolution of the 1-point probability distribution function (PDF) of the dark matter (DM) density field, and the evolution of its moments for fluctuations that are Gaussian in the linear regime.

Methods. We perform numerical simulations of the evolution of the cosmic web for the conventional Λ CDM model. The simulations cover a wide range of box sizes $L = 256 - 4000 h^{-1}$ Mpc, mass and force resolutions and epochs from very early moments $z = 30$ to the present moment $z = 0$. We calculate density fields with various smoothing lengths to find the dependence of the density field on smoothing scale. We calculate PDF and its moments — variance, skewness and kurtosis. We find the dependence of these parameters on the evolutionary epoch z , on the smoothing length R_s , and on the rms deviation of the density field σ , using cubic-cell and top-hat smoothing with kernels $0.4 h^{-1}$ Mpc $\leq R_s \leq 32 h^{-1}$ Mpc.

Results. We focus on the third (skewness S) and fourth (kurtosis K) moments of the distribution functions: their dependence on the smoothing scale R_s , the amplitude of fluctuations σ and the redshift z . Moments S and K , calculated for density fields at different cosmic epochs and smoothed with various scales, characterise the evolution of different structures of the web. Moments, calculated with small-scale smoothing ($R_s \approx (1 - 4) h^{-1}$ Mpc), characterise the evolution of the web on cluster-type scale. Moments, found with large smoothing ($R_s \gtrsim (5 - 15) h^{-1}$ Mpc), describe the evolution of the web on supercluster scale. During the evolution the reduced skewness $S_3 = S/\sigma$ and reduced kurtosis $S_4 = K/\sigma^2$ present a complex behaviour: at a fixed redshift curves of $S_3(\sigma)$ and $S_4(\sigma)$ steeply increase with σ at $\sigma \lesssim 1$ and then flatten out and become constant at $\sigma \gtrsim 2$. If we fix the smoothing scale R_s , then after reaching the maximum at $\sigma \approx 2$, the curves at large σ start to gradually decline. We provide accurate fits for the evolution of $S_{3,4}(\sigma, z)$. Skewness and kurtosis approach at early epochs constant levels, depending on smoothing length: $S_3(\sigma) \approx 3$ and $S_4(\sigma) \approx 15$.

Conclusions. Most of statistics of dark matter clustering (e.g., halo mass function or concentration-mass relation) are nearly universal: they mostly depend on the σ with the relatively modest correction to explicit dependence on the redshift. We find just the opposite for skewness and kurtosis: the dependence of moments on evolutionary epoch z and smoothing length R_s is very different, together they determine the evolution of $S_{3,4}(\sigma)$ uniquely. The evolution of S_3 and S_4 cannot be described by current theoretical approximations. The often used lognormal distribution function for PDF fails to explain even qualitatively the shape and evolution of S_3 and S_4 .

Key words. Cosmology: large-scale structure of Universe; Cosmology: dark matter; Cosmology: theory; Methods: numerical

1. Introduction

According to the presently accepted cosmological paradigm the evolution of the structure in the Universe began from small perturbations which were created during the epoch of inflation. The structure evolved by gravitational amplification to form the cosmic web observed now. It is also accepted that initial density fluctuations were random (though correlated) and had the Gaussian distribution. The Gaussian random field is symmetrical around the mean density, *i.e.* positive and negative deviations from the mean density are equal. On the other hand, it is well known that the present density field of the cosmic web is very asymmetrical: positive density departures from the mean density can be very large while the negative deviations are restricted by the condition that the density cannot be negative. The asymmetry of the density field can be studied with 1-point probability distribution function (PDF) of the density field and its moments.

There are different ways of studying the properties of PDFs. Using analytical methods is one approach (Peebles 1980;

Bernardeau & Kofman 1995; Bernardeau et al. 2002). In this case PDF is modelled theoretically using the cosmological perturbation theory (PT), which allows to calculate PDF and its moments: variance, skewness and kurtosis. Basic elements of cosmological PT and its applications were discussed in detail by Peebles (1980), Bernardeau et al. (2002), and Szapudi (2009). Another possibility is that the evolution of the PDF is calculated numerically by N-body simulations, for early studies see Kofman et al. (1992) and Kofman et al. (1994).

The asymmetry and flatness of the PDF is measured by the third (skewness S) and fourth (kurtosis K) moments of the distribution functions. The moments are the most simple forms of the 3-point and 4-point correlation functions, and as such they cannot be reduced to the second-order statistics such as the correlation function or the power spectrum. In mathematical statistics skewness and kurtosis are defined as dimensionless parameters, and can be called mathematical skewness S and mathematical kurtosis K . They change during the evolution and can be used to characterise changes of the shape of PDF of the density field during the evolution. In cosmology there is a tradition to define skewness and kurtosis in a different way. These skewness

Send offprint requests to: Jaana Einasto, e-mail: jaana.einasto@ut.ee

and kurtosis parameters are called reduced or normalised (Lahav et al. 1993), we shall use the term “cosmological”. During the evolution cosmological skewness S_3 and cosmological kurtosis S_4 remain approximately constant, they characterise general properties of the model of the universe (Peebles 1980).

There exist simple relations between mathematical and cosmological parameters: skewness: $S(\sigma) = S_3 \times \sigma$, and kurtosis $K(\sigma) = S_4 \times \sigma^2$, where σ is the standard deviation of fluctuations of the density field. The initial density field, generated during the inflation, must have density fluctuation with finite non-zero amplitude, $\sigma > 0$, otherwise the structure cannot form. On the other hand, if initial fluctuations were Gaussian, then they should be symmetrical. Thus there exist a question: How the asymmetry in the density distribution evolved?

The goal of this study is to investigate the evolution of the cosmological density distribution function and its moments, and to find relations between parameters defined by mathematical and cosmological methods. We apply the numerical approach, and a broad range of cosmic epochs. We assume that seeds of the cosmic web were created by tiny fluctuations of the early universe in its inflationary phase, and that these fluctuations had a Gaussian distribution. Further we assume that the presently accepted Λ CDM model represents the actual universe so well, that it can be used to investigate the evolution of the structure of the real universe. We perform numerical simulations of the evolution of the cosmic web for the conventional Λ CDM model. To find the evolution we calculate models, corresponding to redshifts from $z = 30$ to the present epoch $z = 0$.

We calculate density fields with various smoothing lengths to find the dependence of properties of the density field on smoothing. We characterise the structure and evolution of the cosmic web by the PDF of the density field, and by its moments, variance, skewness and kurtosis, using both variants of definitions of these parameters, mathematical and cosmological. The information content in mathematical and cosmological variants of PDF moments is identical, however they characterise properties of the cosmic web and its evolution in a different way. In our knowledge this is the first study, where PDF moments are investigated using both definition methods, mathematical and cosmological, in a broad interval of simulation redshifts and smoothing lengths.

The critical step in our study is the smoothing of the density field. Smoothing enables us to select populations of the cosmic web: small-scale smoothing characterises the web on cluster-type scale, large smoothing describes the web on supercluster scale. To characterise the evolution of populations of the cosmic web, we use skewness and kurtosis evolutionary tracks and diagrams. We calculated density fields using three smoothing recipes: B_3 spline, cubic-cell and top-hat smoothing, described in the Appendix A, and found respective moments. The comparison of density fields and moments for different smoothing recipes is given in Appendix B. Sparsity of the density field made results obtained with the B_3 spline unusable, and limited the usable range of smoothing scales for cubic-cell and top-hat smoothing.

The paper is organised as follows. In the next section we describe numerical simulations used and methods to calculate the density field, the PDF of density fields, and method to find its moments – the variance, skewness and kurtosis. In section 3 we analyse basic results. Subsections 3.1 to 3.2 are based on simulations with resolution $N_{\text{grid}} = 512$. Subsection 3.3 and section 4 are based on results obtained with both resolutions. In section 4 we discuss our results and compare numerical results with the evolving pattern of the density field. The last section brings conclusions.

2. Data and methods

In this section we describe our simulations of the evolution of the cosmic web, calculation of the density field, its PDF and moments. Our emphasis is to describe connections between statistical and cosmological definitions of skewness and kurtosis.

2.1. Simulations of the evolution of the cosmic web

To study the evolution of parameters of the cosmological PDF we shall use a three-dimensional grid of input parameters: box size of the simulation, L_0 , smoothing length, R_t , and redshift, z . Smoothing lengths of original density fields from numerical simulation output have a cell size L_0/N_{grid} , where N_{grid} is a parameter, which typically ranges from 500 to 5000. This we call smoothing rank zero. We use a smoothing recipe, which increases the smoothing length by a factor of 2. We use this recipe successively 4 to 5 times. The use of regular sets of box lengths and smoothing lengths yields simulation parameter sets with identical smoothing lengths in units of h^{-1} Mpc. This allows us to compare properties of simulations with identical smoothing lengths, and in this way check convergence of results. Additional test is provided by the regularity of relations: PDF moments vs. redshift z or standard deviation σ . If deviations occur, their reasons can be found by inspecting respective PDFs.

Table 1. Parameters of simulations with the GADGET code

Simulation	L_0	N_p	N_{real}	m_p	R_{min}
(1)	(2)	(3)	(4)	(5)	(6)
L256	256	512 ³	1	0.993	1
L512	512	512 ³	1	7.944	2
L1024	1024	512 ³	1	63.55	4

Notes. Columns give: (1) name of simulation; (2) box size in h^{-1} Mpc; (3) number of particles; (4) number of realisations; (5) mass of a particle in units of $10^{10} h^{-1} M_{\odot}$; and (6) minimal smoothing scale in units of h^{-1} Mpc.

We simulated the evolution of the cosmic web adopting a dark matter (DM) only Λ CDM model, using two sets of simulations. For the first set we use the GADGET code (Springel 2005) with three different box sizes $L_0 = 256, 512, 1024 h^{-1}$ Mpc with $N_{\text{grid}} = 512$. Cosmological parameters for these simulations are $(\Omega_m, \Omega_{\Lambda}, \Omega_b, h, \sigma_8) = (0.28, 0.72, 0.044, 0.693, 0.84)$.

Initial conditions were generated using the COSMICS code by Bertschinger (1995), assuming Gaussian fluctuations. Simulations started at redshift $z = 30$ using the Zeldovich approximation. We extracted density fields and particle coordinates for redshifts $z = 30, 10, 5, 3, 2, 1, 0.5, 0$. Table 1 shows parameters of the simulations. Analysis of the evolution of the power spectra of these simulations is presented in Appendix A.4. We extracted simulation output for eight epochs and used four smoothing scales at each epoch, thus we have all-together $3 \times 8 \times 4 = 96$ sets of simulation parameters.

The second set of simulations is done with the GLAM code (Klypin & Prada 2018), which is a Particle-Mesh code that uses a large grid size N_{grid} . Because GLAM code is much faster than GADGET, we were able to use much better mass resolution and produced many realisations allowing us to reduce effects of the cosmic variance. Different cosmological parameters were used for these simulations: $(\Omega_m, \Omega_{\Lambda}, \Omega_b, h, \sigma_8) = (0.307, 0.693, 0.044, 0.70, 0.828)$. Parameters of GLAM simulations are given in Table 2.

Table 2. Parameters of the simulations with the GLAM code

Simulation	L_0	N_{grid}	N_p	m_p	N_{real}	R_{min}
(1)	(2)	(3)	(4)	(5)	(6)	(7)
GLAM400	400	3000	1500 ³	0.16	8	0.53
GLAM500	500	5000	2000 ³	0.13	24	0.40
GLAM1000	1000	3000	1500 ³	2.52	9	1.33
GLAM1662	1662	5000	2000 ³	4.87	16	1.33
GLAM2000	2000	3000	1500 ³	20.2	9	2.66
GLAM4000	4000	4000	2000 ³	68.2	20	4.00

Notes. Columns give: (1) simulation name; (2) box size L_0 in units of h^{-1} Mpc; (3) number of grid elements; (4) number of particles N_p ; (5) mass of a particle in units of $10^{10} h^{-1} M_\odot$; (6) number of realisations N_{real} ; (7) minimal smoothing scale in units of h^{-1} Mpc.

Simulations started at $z = 100$ using the Zeldovich approximation. For each simulation the smoothing has three ranks. The first rank has cell four times the size of the simulation grid cell L_0/N_{grid} . The second and third ranks have smoothing radii 2 and 4 times larger correspondingly. Simulation outputs were stored at 6 to 17 redshifts in interval $0 \leq z \leq 20$. For each set we found the density field δ in mean density units, calculated its 1-point PDFs and its moments, using smoothing recipes, described below.

2.2. Definitions: dark matter density fields and moments of PDFs

Each N -body simulation provides us with a population of dark matter particles for a box of size L_0 at redshift z . The density field is estimated using a filter of size R_i with the total number of independent elements N . The density field is normalised to the average matter density providing us with the density contrast δ :

$$\delta = \frac{\rho_{\text{DM}}}{\Omega_m \rho_{\text{cr}}} - 1, \quad (1)$$

where Ω_m is the density parameter for the cosmological model and ρ_{cr} is the critical density of the Universe. The density distribution function $P(\delta)$ is defined as a normalised number of elements of the density field with density contrast in the range $[\delta, \delta + d\delta]$:

$$P(\delta) \equiv \frac{\Delta N}{N \Delta \delta}. \quad (2)$$

The second moment of $P(\delta)$ is the rms of the density field:

$$\sigma^2 = \frac{1}{N} \sum_{j=1}^N \delta_j^2 = \langle \delta^2 \rangle, \quad (3)$$

Third and fourth moments of PDF are defined as skewness and kurtosis parameters S and K :

$$S = \frac{1}{N} \sum_{j=1}^N \left(\frac{\delta_j}{\sigma} \right)^3 = \langle \delta^3 \rangle / \sigma^3, \quad (4)$$

and

$$K = \frac{1}{N} \sum_{j=1}^N \left(\frac{\delta_j}{\sigma} \right)^4 - 3 = \langle \delta^4 \rangle / \sigma^4 - 3. \quad (5)$$

The additional term -3 in Eq. (5) makes the value of $K = 0$ for the Gaussian distribution. In statistics it is called excess kurtosis. These definitions are used in mathematical statistics and in many fields of science. Skewness S characterises the degree of asymmetry of the distribution, while kurtosis K measures the presence of heavy tails and peak in the distribution. By definition both are dimensionless quantities (e.g., Kofman et al. 1994; Bernardeau & Kofman 1995).

In the cosmological literature another definition of PDF moments is used (see Peebles 1980; Bernardeau et al. 2002; Szapudi 2009):

$$S_p = \langle \delta^p \rangle / \sigma^{2(p-1)}. \quad (6)$$

where

$$\langle \delta^p \rangle = \int_0^\infty d\delta P(\delta) \delta^p. \quad (7)$$

These moments determine S_p parameters (Bernardeau & Kofman 1995). Specifically, third moment defines the skewness:

$$S_3 = \langle \delta^3 \rangle / \langle \delta^2 \rangle^2, \quad (8)$$

and the fourth moment defines the kurtosis:

$$S_4 = (\langle \delta^4 \rangle - 3\langle \delta^2 \rangle^2) / \langle \delta^2 \rangle^3. \quad (9)$$

The second term in the last equation has the goal to get for Gaussian distribution a value $S_4 = 0$.

Comparing mathematical and cosmological definitions it is easy to see that

$$S = S_3 \times \sigma, \quad (10)$$

and

$$K = S_4 \times \sigma^2. \quad (11)$$

Equations (10) and (11) show that mathematical skewness and kurtosis can be considered as power law functions of standard deviation σ , where cosmological skewness and kurtosis, S_3 and S_4 , play the role of “amplitude” parameters of mathematical S and K .

We calculated smoothed density fields for the first set of models L256, L512 and L1024 using three recipes, the B_3 spline, the cell-cube and the top-hat smoothing. Details of calculations of density fields are explained in the Appendix A. For reasons explained in Appendix A we use for the core analysis results obtained with the cell-cube method.

We calculated for all density fields mathematical skewness S and kurtosis K using Eqs. (4) and (5), and found cosmological skewness S_3 and kurtosis S_4 using Eqs. (10) and (11). The variance σ^2 , the skewness S and the kurtosis K were found with the `moment` subroutine by Press et al. (1992). This subroutine calculates first four moments of PDF. The subroutine calculates also the standard deviation according to the rule: $\text{Var} = 1/(N-1) \sum \delta_j^2$. Our calculations showed that in all cases $\text{Var} = \sigma^2$.

2.3. Definitions: cosmic web populations and their evolutionary tracks

The presence of the cosmic web with clusters, filaments, superclusters, and empty voids is known long ago. For early observational evidence see Gregory & Thompson (1978), Jöeveer & Einasto (1978), Tarenghi et al. (1978), Tully & Fisher (1978)

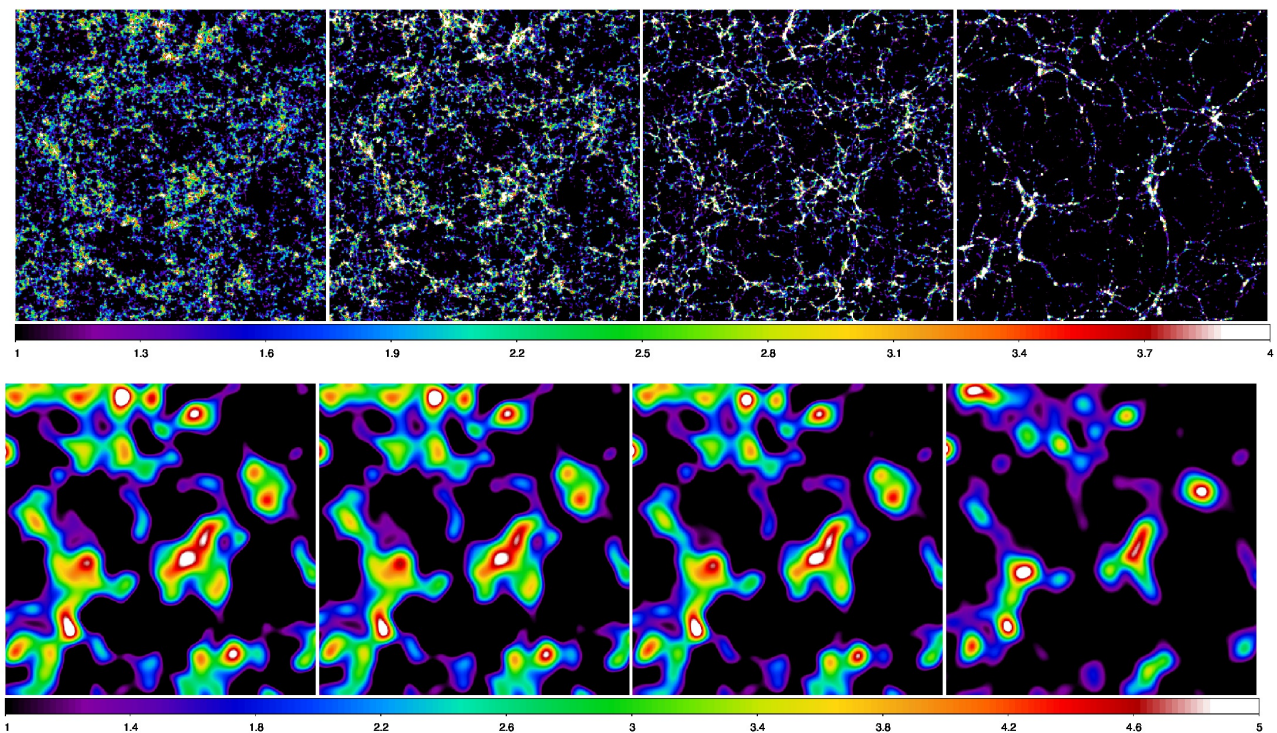


Fig. 1. Density fields of the simulation L256 without additional smoothing and with smoothing length $8 h^{-1}$ Mpc, in upper and bottom panels, respectively. Panels from left to right show fields for epochs $z = 30$, $z = 10$, $z = 3$ and $z = 0$, presented is slices of size $200 \times 200 \times 0.5 h^{-1}$ Mpc. Only over-density regions are shown with colour scales from left to right 1 – 1.4, 1 – 2, 1 – 4, 1 – 8 in upper panels, and 1 – 1.08, 1 – 1.25, 1 – 1.8, 1 – 5 in lower panels.

and de Lapparent et al. (1986); for theoretical explanations see Zeldovich (1970), Zeldovich (1978), Zeldovich et al. (1982), Arnold et al. (1982), Bond et al. (1996), Bond & Myers (1996), Pogosyan et al. (2009), and Cadiou et al. (2020). The basic constituent of the cosmic web is DM, which in the context of classical physics is a collisionless dust of hierarchical fractal distribution (Mandelbrot (1982), Jones et al. (1988)). To select populations of interest to cosmology smoothing is needed. The smoothing scale determines the character of populations. To see the evolution of elements of the cosmic web we consider two main scales: clusters and superclusters.

The growth of structures of various scale during the evolution of the cosmic web is shown in Figure 1. We plot here the density field of the simulation L256 at epochs $z = 30$, $z = 10$, $z = 3$ and $z = 0$. This simulation has the highest resolution and allows to see better the evolution on galaxy up to supercluster scales. Upper panels show the original L256 density fields with cell size $L_0/N_{\text{grid}} = 0.5 h^{-1}$ Mpc, lower panels show the density fields smoothed with length $R_t = 8 h^{-1}$ Mpc, using the B_3 spline with resolution 512^3 . This smoothing method and scale is often used to find superclusters of galaxies, see Liivamägi et al. (2012) and Einasto et al. (2019). We show only over-densities where $D \equiv \delta + 1 \geq 1$.

In upper panels we see the evolution of small-scale elements of the cosmic web — galaxies and clusters of galaxies. During the evolution they merge to form sharp filamentary structure at the present epoch. Such evolution is predicted by theoretical models by Arnold et al. (1982), Bond et al. (1996) and others. In lower panels the evolution of supercluster-scale elements of the cosmic web is shown. We see that superclusters alter their pattern very little during the evolution, only the amplitude of density fluctuations increases.

The density field method is used to select and study various components of the cosmic web: clusters, filaments, superclusters, voids etc. These elements are individual objects, located in different areas of the universe, their volumes do not overlap, but in sum these components fill the whole universe. There exists a large number of various methods to investigate the structure and evolution of such components of the universe, for recent studies see proceedings of the Zeldovich conference by van de Weygaert et al. (2016).

Due to its integrated nature, PDF does not allow to select individual components of the universe. PDF of the density field and its moments are integrated quantities, which characterise properties of the whole web. Objects of various compactness of the cosmic web can be highlighted using smoothing of the density field with different scales. Examples of various smoothing scale were shown in Fig. 1. Smoothing with small lengths, $R_t \leq 1 h^{-1}$ Mpc, highlights the whole cosmic web in the volume under study on scales of halos and subhalos of ordinary galaxies and poor clusters. Medium smoothing lengths, $R_t = 2, 4 h^{-1}$ Mpc, are suited to highlight the cosmic web on scales of rich clusters of galaxies and central regions of superclusters. Large smoothing with $R_t = 8 - 16 h^{-1}$ Mpc highlights the cosmic web on supercluster scale.

Instead of “cosmic web at smoothing scale R_t ” we use the term “populations of the cosmic web”, according to smoothing length, applied to calculate the density field. Populations cover the whole cosmic web, they characterise the web on selected smoothing scale. The smoothing scale is a physical parameter, which allows to highlight the cosmic web at scale of interest. Using various smoothing lengths we can study the hierarchy of structures in the cosmic web.

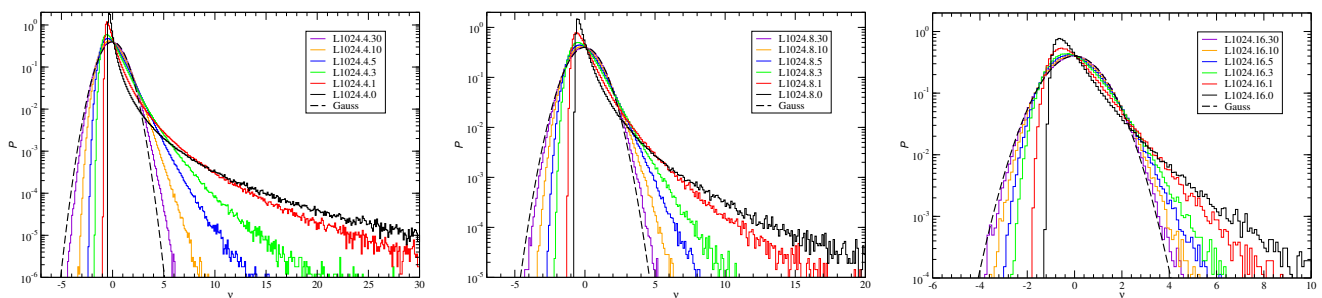


Fig. 2. Density distribution functions $P(\delta)$ as functions of the DM density contrast δ normalized to the rms of density fluctuations $\nu = \delta/\sigma$ for the L1024 simulation smoothed with the cubic-cell method. Panels from left to right are for smoothing lengths $R_t = 4, 8, 16 h^{-1}$ Mpc, indicated as the first index in the simulation name and the redshift coded in the second index. Dashed curves show the Gaussian distribution.

To describe quantitatively the evolution of populations of the cosmic web, we use skewness S and kurtosis K (S_3 and S_4) as functions of the age of the universe, measured by redshift z , or as functions of the rms of the density field, σ . These functions depend on the power spectrum index n , and on other cosmological parameters of the model (Ω_m , Ω_Λ). The simulation epoch, z and the smoothing length, R_t , are parameters. Every simulation of the evolution with fixed values of parameters, z and R_t , yields a dot in evolutionary diagrams.

We call graphs where lines joining simulations with a given smoothing length R_t at various z as “evolutionary tracks” of cosmic web populations, and graphs with lines joining simulations with various smoothing length R_t at a given epoch z as “evolutionary diagrams”. This follows analogy with stellar evolution tracks and HR-diagrams. Evolutionary tracks show how populations of the cosmic web at characteristic scales evolve in the $S(z)$, $K(z)$, $S(\sigma)$, $K(\sigma)$ and $S_{3,4}(z)$, $S_{3,4}(\sigma)$ plots. Evolutionary diagrams show where characteristic populations of the cosmic web are situated in these diagrams at various epochs. Evolutionary tracks and diagrams are based on identical data, only data points are joined by lines differently.

Evolutionary tracks and diagrams display the evolution of the asymmetry of the cosmic web in a simple way. Each plot shows at a glance the growth of the asymmetry of the whole web on different scales.

3. Analysis

In this section we describe the evolution of the cosmic web in the Λ CDM model through its PDF moments. Next we investigate the evolution of variance Var , skewness S and kurtosis K . Thereafter we analyse skewness and kurtosis as functions of rms of the density field σ , and their change with cosmic epoch and smoothing length. These relations are described first for mathematical, and then for cosmological moments. In first subsections we use mostly results obtained with GADGET simulations. In the last subsection we present results obtained with both simulation series.

3.1. Evolution of PDF of Λ CDM simulations

Figure 2 shows the evolution of PDF using the cubic-cell smoothing window. We use as argument the reduced density $\nu = \delta/\sigma$. This presentation is useful to see how well density distributions of our simulations can be represented by a Gaussian distribution. We show density fields of the simulation L1024 using three smoothing lengths $R_t = 4, 8, 16 h^{-1}$ Mpc from left to right panels. PDFs of simulations L512 and L256 are

very similar. Colour coding indicates the evolutionary epoch, $z = 30, 10, 5, 3, 1, 0$.

We see that PDFs of our density fields, obtained with cubic-cell smoothing, are very similar to PDFs, found in previous studies for epochs $z \leq 3$, for an example see Shin et al. (2017). All $P(\nu)$ curves in low-density regions, $\nu \leq 0$, lie below the Gaussian curve, and are in high-density regions, $\nu \geq 5$, above the Gaussian PDF. Such behaviour is expected for PDFs with positive skewness.

Two conclusions are evident from this Figure — (i) PDFs are asymmetric in the sense that high-density regions extend much further than low-density regions; and (ii) smoothing has a dominant role in determining the width of the PDF distribution. Both the asymmetry and the importance of smoothing role of PDFs are known long ago, for early work see Bernardeau (1994), Kofman et al. (1994), and Bernardeau & Kofman (1995). The dependence of PDFs on smoothing length was recently studied by Shin et al. (2017) and Klypin et al. (2018). In our study we see the growth of the asymmetry in a very broad redshift interval, from $z = 30$ to $z = 0$.

3.2. Evolution of the variance, skewness and kurtosis with cosmic epoch z

We present in Fig. 3 dependence of PDF moments of the simulation L512 on the cosmic epoch z . In left panels the dependence is shown for the skewness $S(z)$ and the kurtosis $K(z)$, in right panels for respective cosmological functions $S_3(z)$ and $S_4(z)$. Coloured lines joining symbols are evolutionary tracks of populations of various richness, identified by smoothing lengths. The horizontal axes are inverted to see the evolution from left to right as in following Figures. If we join points at given epochs z , we get evolutionary diagrams, in this representation they are vertical lines.

The variance function $\sigma^2(z)$ is presented in Fig. 4, it is close to the form expected from the halo model. At redshift $z = 30$ simulations at smallest smoothing rank have higher than expected values of the variance, due to difficulties to calculate moments at this redshift and small smoothing length.

The evolution of the skewness $S(z)$ and of the kurtosis $K(z)$ is dominated by the increase of the variance $\sigma^2(z)$ with time. The growth of the skewness $S(z)$ is approximately proportional to the growth of $\sigma(z)$, and the growth of the kurtosis $K(z)$ is proportional to the growth of variance $\sigma^2(z)$. During the evolution from $z = 30$ to $z = 0$ the amplitude of the skewness $S(z)$ increases about 30 times, and that of the kurtosis $K(z)$ by a factor of thousand. The other important aspect is the dependence of amplitudes of skewness and kurtosis curves on the smoothing length R_t . At the present epoch the value of the skewness $S(0)$

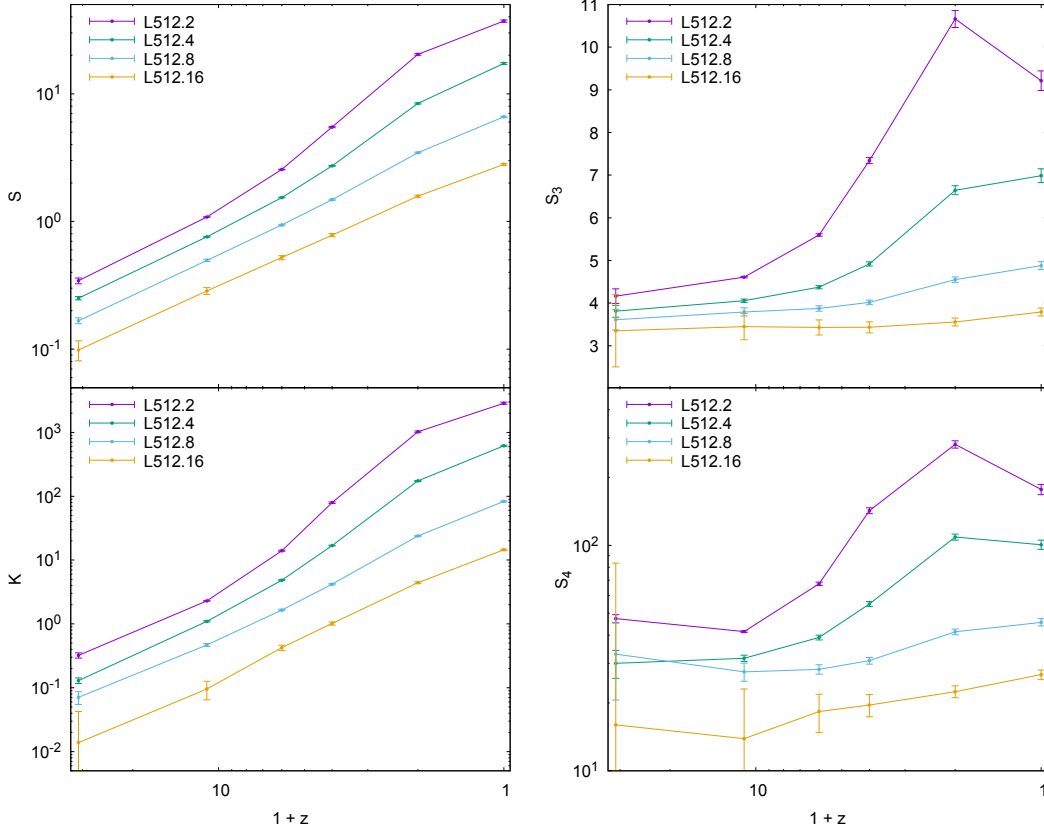


Fig. 3. The dependence of PDF moments on the cosmic epoch z for the simulation L512. *Left top and bottom panels* show the dependence for the skewness $S(z)$ and the kurtosis $K(z)$, respectively, *right panels* are for their cosmological equivalents $S_3(z)$ and $S_4(z)$. Index in simulation name is smoothing length in h^{-1} Mpc.

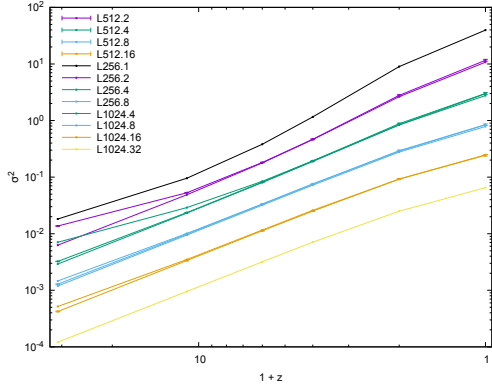


Fig. 4. The dependence of PDF variance σ^2 of GADGET simulations on the cosmic epoch z . Colours indicate smoothing length R_t in h^{-1} Mpc.

is for smoothing length $R_t = 2 h^{-1}$ Mpc ten times higher than for smoothing length $R_t = 16 h^{-1}$ Mpc; the difference in kurtosis $K(0)$ is two orders of magnitudes.

The speed of the evolution of moments can be characterised by the logarithmic gradient, $\gamma_S(z) = d \log S(z) / d \log(1+z)$, for the skewness $S(z)$, and similar equation for the kurtosis $K(z)$. We show in Fig. 5 mean logarithmic gradients of skewness and kurtosis, $\langle \gamma_S \rangle$ and $\langle \gamma_K \rangle$, integrated over the whole redshift range, $0 \leq z \leq 30$, as functions of the smoothing length, R_t . Figures Fig. 3 and Fig. 5 show that negative gradients of the skewness, γ_S , and of the kurtosis, γ_K , change with epoch and smoothing length R_t .

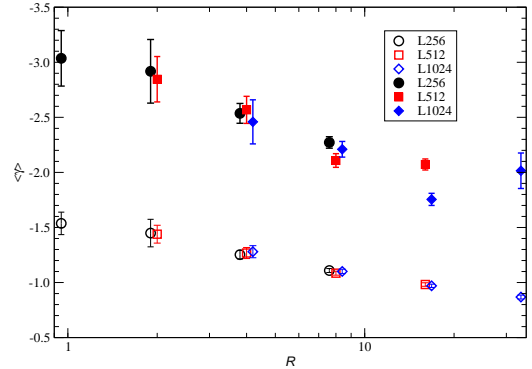


Fig. 5. Mean logarithmic gradients of the skewness, $\langle \gamma_S \rangle$, and the kurtosis $\langle \gamma_K \rangle$, as functions of the smoothing length, R_t . Open symbols are for skewness S , filled symbols for kurtosis K . To help visibility symbols for simulations L256 and L1024 are slightly shifted in R_t coordinate.

The rapid change of the skewness $S(z)$ and the kurtosis $K(z)$ with cosmic epoch z is eliminated by using their cosmological equivalents, $S_3(z)$ and $S_4(z)$, shown in right panels of Fig. 3. Here the dependence of the evolution of the skewness $S_3(z)$ and of the kurtosis $S_4(z)$ on smoothing length R_t is very clearly seen.

We notice that the cosmic epoch z and the smoothing length R_t determine uniquely the position of the model universe in $S(z)$, $K(z)$, $S_3(z)$ and $S_4(z)$ functions, and vice versa: any fixed value

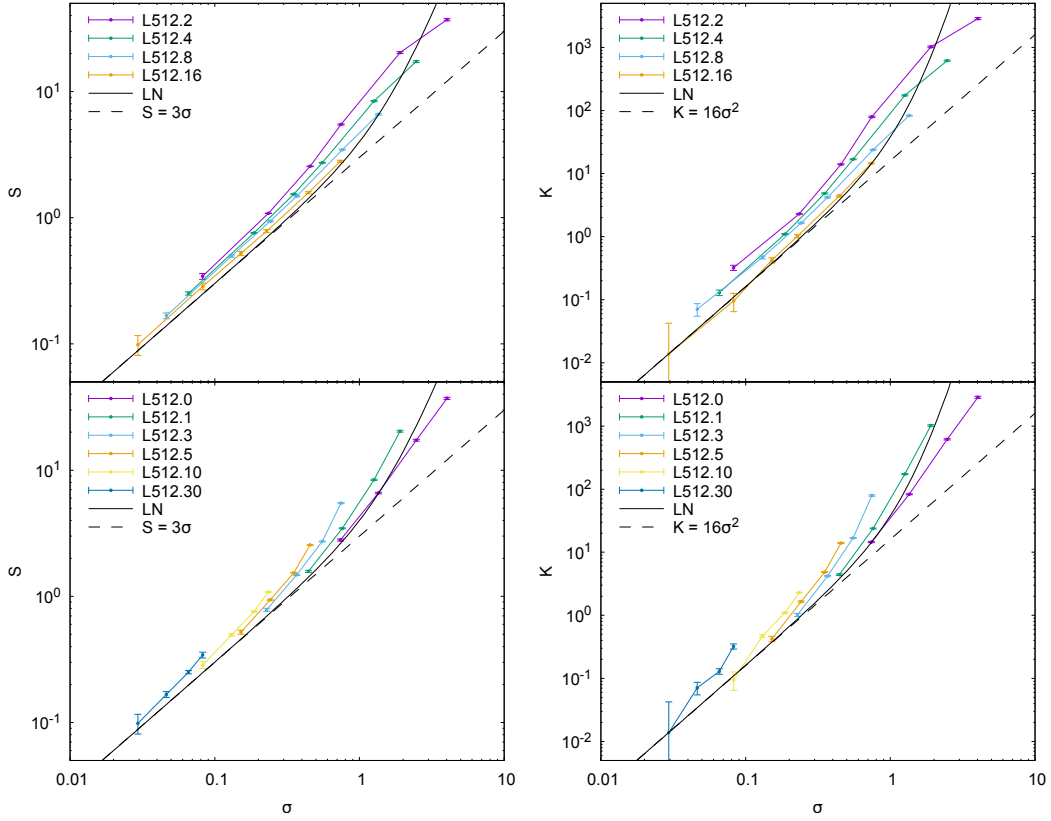


Fig. 6. Evolutionary tracks (top panels) and diagrams (bottom panels) of skewness S (left panels) and kurtosis K (right panels) for the L512 simulation. In top panels the coloured lines join simulations of identical smoothing lengths $R_t = 2, 4, 8, 16 h^{-1}$ Mpc. In the bottom panels curves connect data at the same redshifts $z = 30, 10, 5, 3, 1, 0$. Along lines symbols from top to down correspond to smoothing lengths $2, 4, 8, 16 h^{-1}$ Mpc. Solid bold lines show skewness $S(\sigma)$ and kurtosis $K(\sigma)$ according to the lognormal distribution. Dashed lines show $S = 3\sigma$ and $K = 16\sigma^2$.

of these functions determines uniquely z and R_t parameters of models (for identical cosmological parameters).

3.3. Evolutionary tracks and diagrams of cosmic web populations in $S(\sigma)$ and $K(\sigma)$

In Fig. 3 evolutionary routes of populations are shown using as argument the epoch z . Another possibility to present evolutionary routes is to use as argument instead of z rms of the density field σ . Relations $S(\sigma)$ and $K(\sigma)$ were first investigated by Kofman et al. (1994). We show these relations in Fig. 6 for the L512 simulation, where left panels are for the skewness $S(\sigma)$ and right panels for the kurtosis $K(\sigma)$. In top panels evolutionary tracks are presented, and lines join various populations. In bottom panels evolution diagrams are shown, here simulations of identical age are connected by coloured lines, linking four smoothing lengths, $2, 4, 8, 16 h^{-1}$ Mpc. Error bars are also marked. Other simulations yield similar pictures. Due to differences in resolution, data for the L256 simulation are slightly shifted toward higher σ , and data for the L1024 simulation toward lower σ .

Populations have different values of σ , thus in this representation populations of the same age but different smoothing length are shifted along the σ coordinate. It is remarkable that the shift in σ brings evolutionary tracks of different smoothing lengths to almost coincident, as seen in Figure 6. This coincidence led Kofman et al. (1994) to the conclusion, that a range of σ values could be obtained either by analysing the system at different epochs z or by using different smoothing lengths R_t . As we see later, the dependence of skewness and kurtosis on z and R_t is different.

Figure 6 shows that the overall mean evolution of the skewness $S(\sigma)$ and the kurtosis $K(\sigma)$ is proportional to the first and second power of σ , in accordance with definition Eqs. (10) and (11). The Figure shows also that the evolution on various scales is different. We discuss these differences in more detail in the next subsection.

Figure 6 also shows $S(\sigma) = S_3 \sigma$ and $K(\sigma) = S_4 \sigma^2$ curves for the lognormal PDF distribution with $S_3 = 3 + \sigma^2$ and $S_4 = 16 + 15 \sigma^2 + 6 \sigma^4 + \sigma^6$, see Table 1 of Bernardeau & Kofman (1995). At small rms of the density field, $\sigma \leq 0.5$, the lognormal distributions of $S(\sigma)$ and $K(\sigma)$ are power laws with indices 1 and 2, respectively. On larger σ the lognormal law bends upwards to imitate the dependence of $S(\sigma)$ and $K(\sigma)$ on smoothing length.

3.4. Evolutionary tracks and diagrams of cosmic web populations in $S_3(\sigma)$ and $S_4(\sigma)$

The evolution of skewness $S(\sigma)$ and kurtosis $K(\sigma)$ is dominated by changes in the rms of the density field σ . A much more compact presentation of the evolution is possible when we use cosmological parameters according to definitions Eqs. (10) and (11), $S_3(\sigma) = S(\sigma)/\sigma$ and $S_4(\sigma) = K(\sigma)/\sigma^2$.

This version of evolutionary tracks and diagrams is presented in Figure 7. It is based on data for L512 simulation. We use here two possibilities to highlight the dependence of the evolution on smoothing length and on epoch. In the first case coloured lines join $S_3(\sigma)$ and $S_4(\sigma)$ values for various smoothing lengths, R_t , and we get evolutionary tracks (top panels). Moving along the tracks from left to right we see how the asymmetry and flatness parameters of the cosmic web at given smoothing lengths change

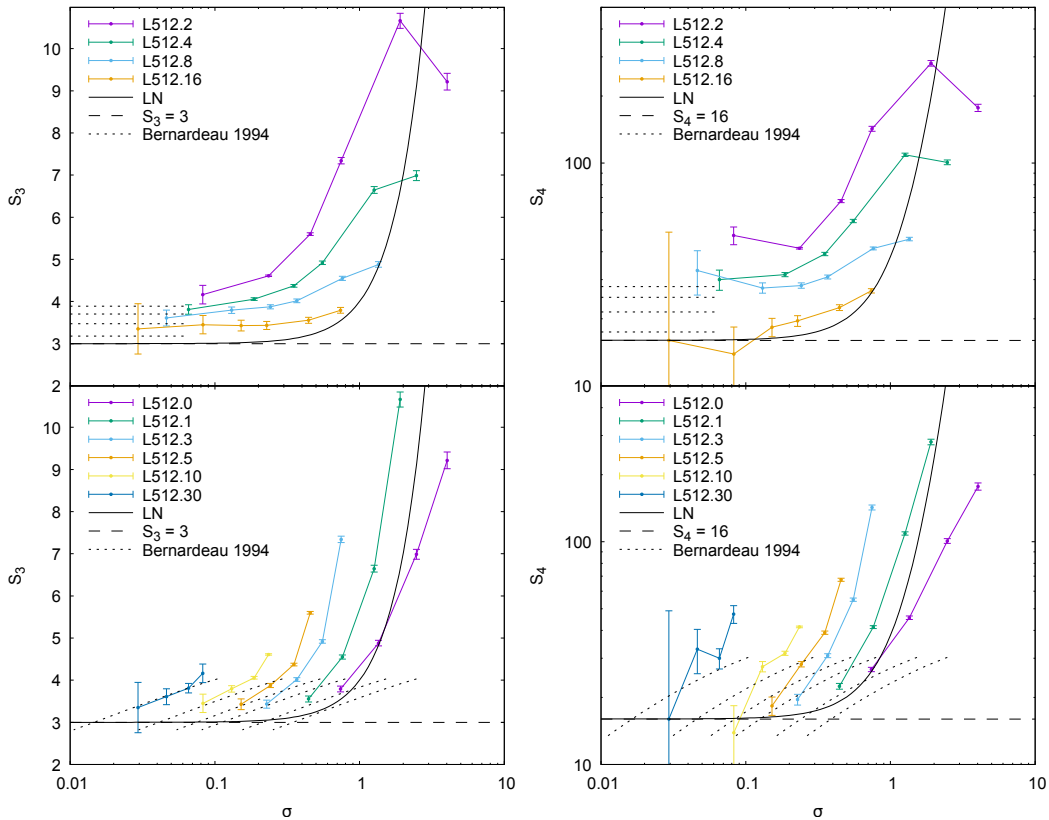


Fig. 7. Evolutionary tracks and diagrams of reduced skewness S_3 (left panels) and kurtosis S_4 (right panels) in simulations L512. Top panels show $S_3(\sigma)$ and $S_4(\sigma)$ for the same smoothing scales. Symbols along tracks from left are for redshifts $z = 30, 10, 5, 3, 1, 0$. In lower panels coloured lines join results of L512 simulations at various cosmic epochs as in Figure 6. The index in the curve name is the redshift z . For each epoch symbols from top to bottom correspond to smoothing lengths 2, 4, 8, 16 h^{-1} Mpc. Solid lines show the reduced skewness S_3 and kurtosis S_4 according to the lognormal distribution. Dashed lines show $S_3 = 3$ and $S_4 = 16$. Dotted lines give perturbation theory limits following the results of Bernardeau (1994).

with redshift. In the second case lines join different $S_3(\sigma)$ and $S_4(\sigma)$ values for various evolutionary epochs, z , and we get evolutionary diagrams (bottom panels).

We discuss first evolutionary tracks of populations for skewness $S_3(\sigma)$ for fixed smoothing length R_t , presented in the top left panel of Figure 7. Populations, selected by $R_t \leq 2 h^{-1}$ Mpc, have maxima $S_3 \approx 11$ at $z \approx 2$, and decrease of S_3 for later epochs, $z \leq 2$. Populations, selected by smoothing length $R_t = 4 h^{-1}$ Mpc, and shown by green lines, reach at present epoch amplitudes $S_3 \approx 7$. Populations, selected by smoothing length $R_t = 8 h^{-1}$ Mpc, have a moderate increase of the $S_3(\sigma)$, shown by dark blue lines. A similar increase was found by Shin et al. (2017) for epochs $z \leq 4$, see their Figure 4. Authors used top-hat smoothing with $R_t = 10 h^{-1}$ Mpc. Populations, selected by smoothing length $R_t = 16 h^{-1}$ Mpc, have during the evolution approximate constant $S_3(\sigma)$ levels, see the orange line in top left panel of Figure 7.

Evolutionary tracks of the kurtosis $S_4(\sigma)$ are shown in the top right panel of Figure 7. The general shape of tracks is similar, only the growth of $S_4(\sigma)$ for small smoothing lengths and late epochs is much larger. $S_4(\sigma)$ evolutionary tracks are more influenced by errors, both sampling errors, shown as errorbars in Figure 7, and possible systematic errors, discussed in the Appendix B. When we take these possible errors into account, we see that evolutionary tracks of $S_3(\sigma)$ and $S_4(\sigma)$ of populations with different smoothing lengths are well separated from each other. Intervals between lines for various smoothing lengths are quite regular. This shows that the increase of $S_3(\sigma)$ and $S_4(\sigma)$

with the decreasing smoothing length is a general property of the evolution.

Bottom panels in Figure 7 show evolution diagrams of populations for simulation L512: lines joining symbols connect simulations of identical redshift z . As in Figure 6, for each epoch symbols from top to down correspond to smoothing lengths $R_t = 2, 4, 8, 16 h^{-1}$ Mpc. We see that evolution diagrams for different ages are well separated from each other, and are located at approximately similar mutual distances along σ -axis. This conclusion is valid for both $S_3(\sigma)$ and $S_4(\sigma)$.

We show in all panels by dotted lines $S_3(\sigma)$ and $S_4(\sigma)$ functions, as given by PT by Bernardeau (1994), for the same set of smoothing lengths and redshifts. The comparison shows that for redshift $z = 30$ PT is in fairly good agreement with results of numerical simulations. For smaller redshift PT is not able to reproduce $S_3(\sigma)$ and $S_4(\sigma)$ functions, found from simulations. Differences increase with the decrease of smoothing length.

Figure 8 shows results of GLAM simulations for skewness $S_3(\sigma)$ and kurtosis $S_4(\sigma)$. Here we combine data from all six GLAM simulations, all with many realisations, thus the shot noise is much smaller. Data for different boxes agree quite well within 2 – 3 %. In top panels coloured lines join simulations with identical smoothing lengths, in bottom panels simulations of identical redshift, *i.e.* we have evolutionary tracks and diagrams, respectively.

Evolutionary tracks of populations are seen in great details, especially for populations with small smoothing lengths. At lowest smoothing length peaks of $S_3(\sigma)$ and $S_4(\sigma)$ are at redshift

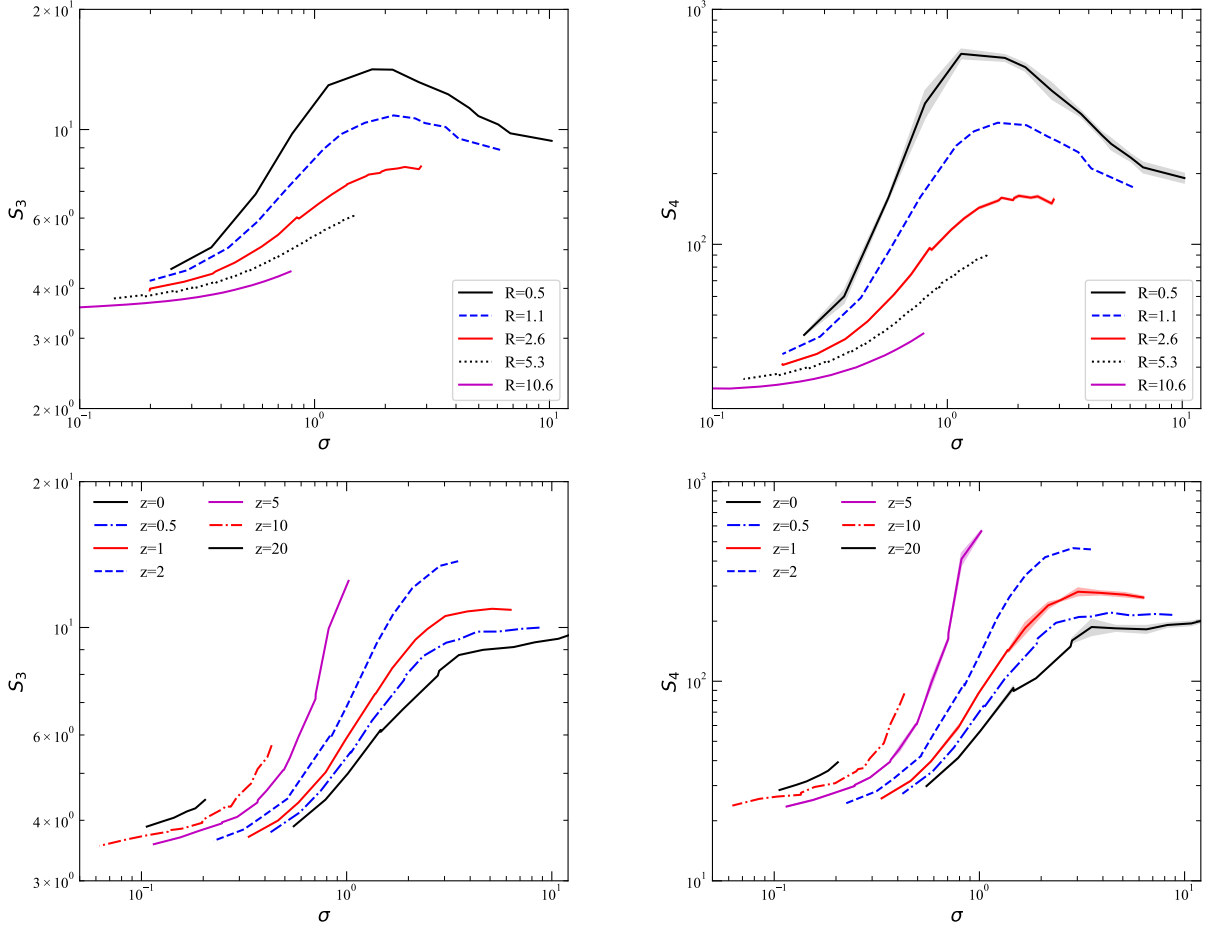


Fig. 8. Evolutionary tracks and diagrams of skewness S_3 (left panels) and kurtosis S_4 (right panels). Top panels show $S_3(\sigma)$ and $S_4(\sigma)$ for the same smoothing scales. Bottom panels show how $S_3(\sigma)$ and $S_4(\sigma)$ change with the redshift. Shaded areas correspond to 1σ statistical uncertainties.

$z = 5$, followed by slow decrease at smaller redshifts. The evolution is shown for five smoothing lengths from $R_l = 0.5 h^{-1} \text{ Mpc}$ to $R_l = 10.6 h^{-1} \text{ Mpc}$. Moving along tracks from left to right we see changes of $S_3(\sigma)$ and $S_4(\sigma)$ during the evolution from $Z = 10$ to $z = 0$. In this Figure points for various redshifts are not marked.

Evolutionary diagrams are calculated for seven redshifts, starting from $z = 20$. Lower tips of curves correspond in most cases to smoothing length $R_l = 10.6 h^{-1} \text{ Mpc}$, upper tips are for lowest smoothing length $R_l = 0.5 h^{-1} \text{ Mpc}$. Figure 8 shows that evolutionary diagrams have a more complex structure than expected from simulations with lower resolution. For smaller smoothing lengths, $R_l \leq 2 h^{-1} \text{ Mpc}$, and recent epochs, $z \leq 1$, diagrams reach constant levels. All curves, both for changing z and R_l , yield monotonic ladders without crossing each other. In general, GLAM simulations confirmed all basic findings from the GADGET simulations with high confidence, and suggested some important details, not seen in simulations with low mass resolution.

Results presented in Figures 7 and 8 show an interesting and somewhat counter-intuitive features: at the same rms of fluctuations σ the deviations from the Gaussian distribution are larger at high redshifts z . One naively should expect that, as the fluctuations grow, the PDF should become more non-Gaussian. However, at first sight it goes other way around. For example, in the top panels of Figure 8 the factors S_3 and S_4 decrease with decreasing of redshift at fixed σ .

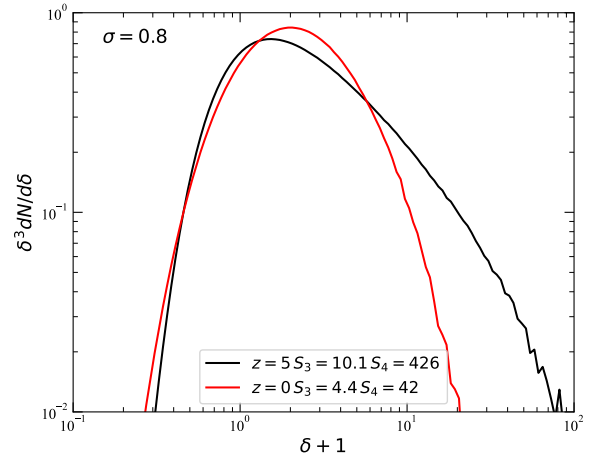


Fig. 9. Comparison of the PDFs with the same rms fluctuations $\sigma = 0.8$ but estimated at different redshifts $z = 0$ and $z = 5$. PDFs are scaled with δ^3 to reduce the dynamical range. Filtering scales are $R_l = 10 h^{-1} \text{ Mpc}$ at $z = 0$ and $R_l = 0.5 h^{-1} \text{ Mpc}$ at $z = 5$.

In order highlight this effect, in Figure 9 we plot PDFs selected at two different redshifts that have the same $\sigma = 0.8$. It is clear that at $z = 5$ the PDF is much broader and more evolved than at $z = 0$. The key issue here is that the filtering scale R_l is dramatically different for $z = 5$ and $z = 0$. Indeed, in or-

der to have the same σ at high redshift, one needs to decrease the filtering scale. In our case that amounts to changing R_f from $10 h^{-1}$ Mpc at $z = 0$ to $0.5 h^{-1}$ Mpc at $z = 5$. With much smaller filtering scale at $z = 5$ we are probing the power spectrum of fluctuations $P(k)$ at much larger wavenumbers k where the shape of the power spectrum is quite different from that on small k . Or in different terms: at redshift $z = 5$ small-scale structures of the cosmic web, highlighted by smoothing with $R_f = 0.5 h^{-1}$ Mpc, are more asymmetric than supercluster-scale structures at the present epoch.

This effect becomes quite obvious once we understand why this happens. However, it presents a problem for non-linear models of PDF such as the lognormal distribution where the rms of density perturbation σ is the only factor defining the PDF. These models cannot possibly account for the evolution of PDF with the redshift.

4. Discussion

In this section we discuss the growth of density fluctuations and the evolution of particle densities using theoretical models. Thereafter, we compare our results with earlier ones. Finally we discuss the cosmological interpretation of our data.

4.1. Comparison with theoretical models

An important conclusion from our data is that the dependencies of PDF moments on evolutionary epoch z and on smoothing length R_f are very different. Figures 7 and 8 demonstrate clearly that rms of density fluctuations σ does not determine moments of PDF in a unique way. At a fixed redshift the S_3 and S_4 curves increase with σ at small $\sigma \lesssim 1$ then flatten out and stay constant at $\sigma \gtrsim 2$. The behaviour is different for fixed R_f . At small σ the curves go up, but then they reach a maximum and start to decline. Note that regardless of the selection (constant z or constant R_f) the curves show a complex behaviour. For example, position and amplitude of the maximum of S_3 change with R_f , if R_f is fixed. For fixed z the amplitude and the redshift z of the plateau depend on the redshift.

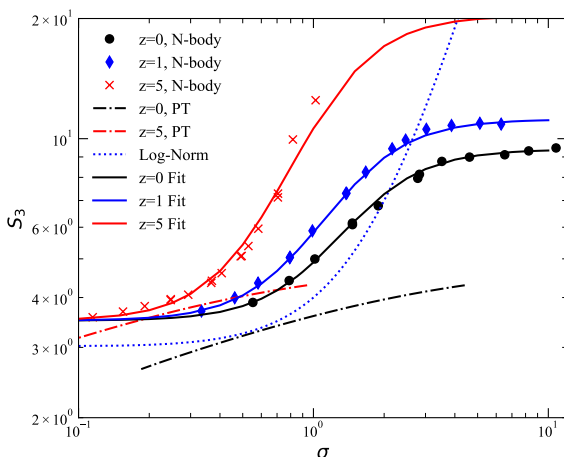


Fig. 10. Comparison of $S_3(\sigma, z)$ for redshifts $z = 0, 1, 5$ as predicted by N -body simulations with predictions by the perturbation theory (PT) and the lognormal distribution.

In Figure 10 we compare the evolution of $S_3(\sigma)$ of the GLAM simulations with results of the PT, the lognormal distribution and an analytical fit. The new analytical fit uses as input

σ and redshift z and gives S_3 and S_4 using a 4 free parameter approximation. It does a pretty good job and can be useful for predictions. The lognormal and PT results are not very accurate. The lognormal distribution does not have any dependence on redshift because by design it is a function of σ only. It fails on all scales – small and large σ and even at high redshifts. PT approximation predicts some evolution with the redshift, but the magnitude of the effect is just too small.

4.2. Comparison with earlier results

The tradition to quantify moments of the PDF using Eq. (8) and (9) goes back to Peebles (1980). Based on the linear perturbation theory Peebles found that in an Einstein-de Sitter model with $\Omega = 1$ the cosmological skewness has the value $S_3 = 34/7$. Later studies showed that it depends also on the effective index n of the power spectrum, $P(k) \propto k^n$, as well as on smoothing length R (Bouchet & Hernquist 1992; Bouchet et al. 1992), (Juszkiewicz et al. 1993; Bernardeau 1994). Following studies of PDF and its moments have confirmed and extended these results, see among others Catelan & Moscardini (1994), Bernardeau & Kofman (1995), Juszkiewicz et al. (1995), Lokas et al. (1995), Gaztanaga & Bernardeau (1998), Gaztañaga et al. (2000), Kayo et al. (2001) and Uhlemann et al. (2017). These studies were basically theoretical, using various methods of the perturbation theory to follow the evolution of PDFs of the density field and its moments.

Kofman et al. (1994) investigated the evolution of 1-point distributions from Gaussian initial fluctuations. Authors approximated the evolution using Zeldovich formalism in the limit of laminar flow. They found that the PDF of the density field rapidly obtains the lognormal shape. Authors also noticed that moments of the density gradually deviate from Gaussian in the whole range of σ tested. Authors used numerical simulations to find PDFs for various epochs and smoothing radii, see Figure 5 by Kofman et al. (1994). We summarise results from different simulations in Table 3. Bernardeau & Kofman (1995) found that the growth of σ is very similar to the prediction of linear theory: $\sigma \propto a$, where a is the scale factor; see their Figs. 9 and 11. Authors notice that faster nonlinear growth in high-density regions is compensated for by the slower deepening of PDF in low-density regions.

Various theoretical approximations were suggested to find values of cosmological skewness and kurtosis parameters. Bernardeau & Kofman (1995) list in their Table 1 values of cosmological skewness S_3 and kurtosis S_4 for various approximations. Depending on the approximation, S_3 and S_4 values depend on the index n of the power spectrum differently. Using analytical methods authors calculated the dependence of PDF moments on σ and high-end cutoff of PDF.

Marinoni et al. (2008) used the VIMOS VLT Deep Survey by Marinoni et al. (2005) over the redshift range $0.7 < z < 1.5$ at scale $R = 10 h^{-1}$ Mpc, and find that the skewness decreases with increasing redshift $2.0 \geq S_3 \geq 1.3$, in good agreement with prediction by Fry & Gaztanaga (1993).

Romeo et al. (2008) investigated discreteness effects in Λ CDM simulations and their effects to cosmological parameters, standard deviation σ , skewness S , and kurtosis K . Their simulation box has size $L = 20 h^{-1}$ Mpc, divided into 128^3 cells, and populated with $N = 16^3, 32^3, \dots, 256^3$ particles, smoothed with various smoothing rules: top-hat, “cloud-in-cell”, “triangular shaped cloud”. Moments depend on the number of particles in cells. For the present epoch, $z = 0$, $\sigma \approx 20$, $S \approx 120$,

Table 3. Estimations of skewness and kurtosis parameters

Author	Model	Box size L_0 h^{-1} Mpc	Redshift interval	R_t h^{-1} Mpc	Moments
Kofman et al. (1994)	SCDM	200	$0.5 \geq a \geq 1.0$	5 – 21	S, K
Romeo et al. (2008)	Λ CDM	20	$15 \leq z \leq 0$	$\ll 1$	S, K
Hellwing et al. (2010)	SCDM, Λ CDM, ReBEL	180 - 1024	$5 \leq z \leq 0$	1 – 100	$S_3 - S_8$
Mao et al. (2014)	Λ CDM	2400	$z = 0$	10 – 100	S_3, S_4
Shin et al. (2017)	Λ CDM	1024	$4 \leq z \leq 0$	2 – 25	S_3, S_4
Hellwing et al. (2017)	Λ CDM, nDGP	1024	$1 \leq z \leq 0$	1 – 100	$S_3 - S_8$
This work	Λ CDM	256 - 4000	$30 \leq z \leq 0$	0.4 – 32	S, K, S_3, S_4

$K \approx 2.5 \times 10^4$. Such high values are expected for a smoothing kernel of size $R_t \ll 1 h^{-1}$ Mpc.

Hellwing & Juszkiewicz (2009) used numerical simulations to investigate the role of long-range scalar interactions to the DM model. As tests authors studied the power spectrum, correlation function and PDF of various models. Redshift evolution was studied in the interval $5 \leq z \leq 0$. Hellwing et al. (2010) used a series of N-body simulations to test the Λ CDM and modified DM model ReBEL. Basic data on models are given in Table 3. Initial redshifts varied between $80 \leq z_{ini} \leq 30$, snapshots were stored for $5 \leq z \leq 0$. Density fields were calculated with top-hat windows of radii up to $100 h^{-1}$ Mpc. Models were compared using cosmological moments of the density field, S_3, \dots, S_8 . Hellwing (2010) studied the influence of long-range scalar DM interactions to properties of galactic halos. Hellwing et al. (2017) continued the comparison of Λ CDM and modified DM model – normal branch Dvali-Gabadadze-Porrati (nDGP) gravity models with mild and strong growth rate enhancement. Data on simulations are given in Table 3.

Pandey et al. (2013) investigated the evolution of the density field of Millennium and Millennium II simulations, which have higher spatial resolution than our GADGET simulations. The density distribution in Millennium simulations is shown in Figure 4 by Pandey et al. (2013). It is very similar to distribution of particle densities in our simulations in the present epoch, only due to better resolution high- and low-density tails are better represented.

Mao et al. (2014) used N-body simulations to investigate whether measurements of the PDF moments can yield constraints on primordial non-Gaussianity. Authors find the dependence of standard deviation σ , cosmological skewness S_3 and cosmological kurtosis S_4 , using smoothing radii $R_t = 10 - 100$. All moments decrease with increasing smoothing length R_t ; for smoothing spheres of radii $R_t = 10 - 100 h^{-1}$ Mpc authors find, $2.5 \leq S_3 \leq 4$, and $5 \leq S_4 \leq 30$.

Shin et al. (2017) found a new fitting formula for PDF, which describes the density distribution better than the lognormal one. Parameters of the fitting formula were found on the basis of numerical simulations for various input cosmological simulations in the interval of cosmic epochs $z \leq 4$.

4.3. Cosmological interpretation

4.3.1. Contrasting evolution of the cosmic web on small and large scales

One of the findings of our study is the contrast between the evolution of the cosmic web on small and large scales, as defined by smoothing length R_t . Cosmic web populations, defined by large smoothing length, $R_t \geq 10 h^{-1}$ Mpc, have at all cosmic epochs

$S_3 \leq 4$ and $S_4 \leq 35$. Cosmic web populations, defined by small smoothing length, $R_t \leq 2 h^{-1}$ Mpc, have in late evolutionary epochs, $z \leq 5$, maxima of moments $S_3 \geq 10$ and $S_4 \geq 150$.

To understand the reason for this difference we have to remember, that reduced moments S_3 and S_4 are actually amplitude parameters of mathematical skewness $S = S_3 \times \sigma$ and kurtosis $K = S_4 \times \sigma^2$, as defined by Eqs. (10) and (11). Data, presented in Figs. 7 and 8, can be expressed as functions of redshift of the mathematical skewness $S(z)$ and kurtosis $K(z)$, as done in Fig. 3. We see that evolution of large-scale populations of the cosmic web proceeds with almost constant rate, measured by mean logarithmic gradients, $\langle \gamma_S \rangle \approx -1$ and $\langle \gamma_K \rangle \approx -2$, shown in Fig. 5. The speed of the evolution of small-scale elements, characterised by small smoothing length R_t , is much faster: for $R_t = 1 h^{-1}$ Mpc $\langle \gamma_S \rangle \approx -1.5$ and $\langle \gamma_K \rangle \approx -3$, see Fig. 5.

The increase of the (negative) gradient in the interval $z \leq 10$ is due to the non-linear growth of density perturbations, important for small-scale perturbations. The relative decrease of the gradient for $z \leq 1$ is due to the influence of the Λ term.

4.3.2. Similarity of the evolution of skewness and kurtosis

We note one important property of PDFs of the cosmic web: the shapes of $S_3(\sigma)$ and $S_4(\sigma)$ curves are qualitatively very similar, as seen in Fig. 7 and especially in Fig. 8. This property is due to the character of density field of the cosmic web — it is very asymmetric, all details of the structure are in over-density regions, and the under-density region is almost structure-less. We conclude that both PDF moments, the skewness $S(\sigma)$ and the kurtosis $K(\sigma)$ (and their amplitudes $S_3(\sigma)$ and $S_4(\sigma)$) measure essentially the asymmetry of the density field. However, there exist large quantitative differences: at maximum $S_4(\sigma)$ is larger than $S_3(\sigma)$ by a factor of about 50.

4.3.3. Independent evidence for the asymmetry of density field

The asymmetry of the evolution of density perturbations is reflected not only in the PDF of the density field, as measured by the skewness parameter S . It is seen also in the distribution of particle densities, as shown by Pandey et al. (2013). Asymmetry is observed also in the distribution of the number of superclusters as function of the reduced density, $\nu = \delta/\sigma$, see Figure 1 by Einasto et al. (2019) and Figure 2 by Einasto et al. (2021).

According to our assumptions the evolution of the universe started from a Gaussian random field, which is symmetrical around the mean density, *i.e.* positive and negative deviations from the mean density are equal. Thus we can ask: When the density field became asymmetric?

To explore the problem let us have a look to the evolution of the structure shown in Figure 1. We see that, for example, supercluster-type elements are visible almost in the same form already at the earliest epoch, $z = 30$, and change little during the late stage of the evolution. Cluster-type elements are also seen in the early universe, but they change much during the evolution. These differences illustrate numerical data of the evolution on various scales, shown in Figure 7. What is important for the present study is the presence of both small- and large-scale elements of the cosmic web already at early stages of the evolution.

Another manifestation of the early evolution of the cosmic web is the almost constant number of superclusters during the evolution, see Figure 2 by Einasto et al. (2019) and Figure 6 by Einasto et al. (2021). This suggests that supercluster embryos were created in very early universe, much earlier than seen in the density field of the cosmic web at redshift $z = 30$. The difference between positive and negative density perturbations lies in the fact, that positive perturbations form distinct structures, embryos of galaxies, clusters and superclusters, already in the very early stages of the evolution, whereas similar strength negative perturbations form voids and act as repellers. Asymmetry parameter, mathematical skewness S , measures this difference in positive and negative perturbations.

4.3.4. PDF moments in the early universe

Of interest is the behaviour of skewness and kurtosis at very early epochs. Figs. 7 and 8 show, that all $S_3(\sigma)$ and $S_4(\sigma)$ curves approach with increasing z limiting values, depending on the scale of systems, as determined by smoothing length. In this way our analysis confirmed earlier results by Bernardeau & Kofman (1995), Hellwing et al. (2010, 2017), Mao et al. (2014).

Presently we cannot answer the question: How PDF moments $S(\sigma)$, $K(\sigma)$, $S_3(\sigma)$ and $S_4(\sigma)$ behave at very small σ ? The cosmic density field can have small rms of density fluctuations σ in a young universe at high redshift z , or using a very large smoothing length R_t . Our data suggest that in a young universe PDF moments converge with increasing z to limits $S(\sigma) = S_3(\sigma)$, and $K(\sigma) = S_4(\sigma)$ with $S_3 \approx 3$ and $S_4 \approx 15$. The limited range of smoothing lengths R_t used in our simulations gives no hint to $S_3(\sigma)$ and $S_4(\sigma)$ for very large smoothing. Future studies are needed to solve this question.

4.3.5. Early evolution of the universe

The early evolution of the density field is calculated in simulations using the Zeldovich approximation, thereafter actual numerical simulations follow. Available data suggest that embryos of galaxies and superclusters were created by high peaks of the initial field. The initial velocity field around peaks is almost laminar. Highest density peaks of the density field started to attract surrounding matter stronger than around peaks of lower density. In this way centres of future galaxies, clusters and superclusters formed. The almost identical pattern of the cosmic web on supercluster scale at epochs with $z \geq 3$ suggests that the same pattern existed at earlier epochs, actually soon after the creation of density fluctuations. The development of the density field in the early phase is well described by Zeldovich (1970) approximation and its extension, the adhesion model by Kofman & Shandarin (1988). As shown by Kofman et al. (1990, 1992), the adhesion approximation yields for the present epoch structures, very similar to structures, calculated by N-body numerical simulations of the evolution of the cosmic web with the same initial fluctua-

tions. Thus the combination of theoretical models and numerical simulations suggests that the asymmetry of the PDF started to form soon after the creation of fluctuations in the early period of the evolution of the universe.

5. Conclusions

We study the evolution of the DM density field with the goal to find evolutionary changes in 1-point PDF and its moments. We use a large set of input parameters of N -body simulations – the box size, L_0 , smoothing length, R_t , and simulation epoch, z , to follow the evolution of Λ CDM models. We perform numerical simulations of Λ CDM models for two sets of simulations, one with $N_{\text{grid}} = 512$, and the other with $N_{\text{grid}} = 2000, 5000$. In these sets we used different cosmological parameters, simulation algorithms, and simulation box sizes. We calculated density fields for several series of smoothing lengths, using various smoothing rules. For all simulation sets we calculated 1-point PDFs and its moments: standard deviation σ , skewness and kurtosis. The present study extends previous ones by analysing both mathematical and cosmological skewness and kurtosis, using a wide range of evolutionary epochs from $z = 30$ on, and a wide range of smoothing lengths from $R_t = 0.4$ to $R_t = 32h^{-1}$ Mpc. We defined populations of the cosmic web by the smoothing length R_t , used to calculate PDF moments.

The basic conclusions of our study are as follows.

1. Moments S and K , calculated for density fields at different cosmic epochs and smoothed with various scales, characterise the evolution of different structures of the web. Moments, calculated with small-scale smoothing ($R_t \approx (1 - 4) h^{-1}$ Mpc), characterise the evolution of the web on cluster-type scale. Moments, found with large smoothing ($R_t \gtrsim (5 - 15) h^{-1}$ Mpc), describe the evolution of the web on supercluster scale.
2. During the evolution the reduced skewness $S_3 = S/\sigma$ and reduced kurtosis $S_4 = K/\sigma^2$ present a complex behaviour: at a fixed redshift curves of $S_3(\sigma)$ and $S_4(\sigma)$ steeply increase with σ at $\sigma \lesssim 1$ and then flatten out and become constant at $\sigma \gtrsim 2$. If we fix the smoothing scale R_t , then after reaching the maximum at $\sigma \approx 2$, the curves at large σ start to gradually decline. We provide accurate fits for the evolution of $S_{3,4}(\sigma, z)$. Skewness and kurtosis approach at early epochs constant levels: depending on smoothing length: $S_3(\sigma) \approx 3$ and $S_4(\sigma) \approx 15$, respectively.
3. Direct and indirect data suggest that seeds of elements of the cosmic web were created at early epoch at inflation and started to grow thereafter. This explains the continuous growth of asymmetry of the density distribution, expressed by the skewness S and kurtosis K functions.

Our study showed that the evolution of S_3 and S_4 cannot be described by current theoretical approximations. The often used lognormal distribution function for PDF fails to explain even qualitatively the shape and evolution of S_3 and S_4 . We still have no definite answer to the question: How PDF moments behave at very small σ ? The cosmic density field has small rms of density fluctuations in a young universe, and in the universe at the present age applying very large smoothing length of the density field. The limited range of smoothing lengths used in our simulations gives no hint to S_3 and S_4 for very large smoothing.

Acknowledgements. We thank Ivan Suhhonenko for performing GADGET simulations, used in this study, Enn Saar for discussion, and anonymous referee for very stimulating suggestions, which helped in improve the paper. This work was

supported by institutional research funding IUT40-2 of the Estonian Ministry of Education and Research, by the Estonian Research Council grant PRG803, and by Mobilias Plus grant MOBT75. We acknowledge the support by the Centre of Excellence “Dark side of the Universe” (TK133) financed by the European Union through the European Regional Development Fund.

References

- Arnold, V. I., Shandarin, S. F., & Zeldovich, I. B. 1982, *Geophysical and Astrophysical Fluid Dynamics*, 20, 111
- Bernardeau, F. 1994, *ApJ*, 433, 1
- Bernardeau, F., Colombi, S., Gaztañaga, E., & Scoccimarro, R. 2002, *Phys. Rep.*, 367, 1
- Bernardeau, F. & Kofman, L. 1995, *ApJ*, 443, 479
- Bertschinger, E. 1995, *ArXiv:astro-ph/9506070* [[arXiv:astro-ph/9506070](#)]
- Bond, J. R., Kofman, L., & Pogosyan, D. 1996, *Nature*, 380, 603
- Bond, J. R. & Myers, S. T. 1996, *ApJS*, 103, 1
- Bouchet, F. R. & Hernquist, L. 1992, *ApJ*, 400, 25
- Bouchet, F. R., Juszkiewicz, R., Colombi, S., & Pellat, R. 1992, *ApJL*, 394, L5
- Cadiou, C., Pichon, C., Codis, S., et al. 2020, *MNRAS*, 496, 4787
- Catelan, P. & Moscardini, L. 1994, *ApJ*, 426, 14
- Davison, A. C. & Hinkley, D. V. 1997, *Bootstrap Methods and Their Application* (Cambridge University Press, Cambridge, UK)
- de Lapparent, V., Geller, M. J., & Huchra, J. P. 1986, *ApJL*, 302, L1
- Efron, B. 1982, *The Jackknife, the Bootstrap and other resampling plans*
- Einasto, J., Hütsi, G., Suhhonenko, I., Liivamägi, L. J., & Einasto, M. 2021, *A&A*, 647, A17
- Einasto, J., Suhhonenko, I., Liivamägi, L. J., & Einasto, M. 2019, *A&A*, 623, A97
- Fry, J. N. & Gaztanaga, E. 1993, *ApJ*, 413, 447
- Gaztañaga, E., Fosalba, P., & Elizalde, E. 2000, *ApJ*, 539, 522
- Gaztanaga, E. & Bernardeau, F. 1998, *A&A*, 331, 829
- Gregory, S. A. & Thompson, L. A. 1978, *ApJ*, 222, 784
- Hellwing, W. A. 2010, *Annalen der Physik*, 19, 351
- Hellwing, W. A. & Juszkiewicz, R. 2009, *Phys. Rev. D*, 80, 083522
- Hellwing, W. A., Juszkiewicz, R., & van de Weygaert, R. 2010, *Phys. Rev. D*, 82, 103536
- Hellwing, W. A., Koyama, K., Bose, B., & Zhao, G.-B. 2017, *Phys. Rev. D*, 96, 023515
- Jöeveer, M. & Einasto, J. 1978, in *IAU Symposium, Vol. 79, Large Scale Structures in the Universe*, ed. M. S. Longair & J. Einasto, 241–250
- Jing, Y. P. 2005, *ApJ*, 620, 559
- Jones, B. J. T., Martinez, V. J., Saar, E., & Einasto, J. 1988, *ApJL*, 332, L1
- Juszkiewicz, R., Bouchet, F. R., & Colombi, S. 1993, *ApJL*, 412, L9
- Juszkiewicz, R., Weinberg, D. H., Amsterdamski, P., Chodorowski, M., & Bouchet, F. 1995, *ApJ*, 442, 39
- Kayo, L., Taruya, A., & Suto, Y. 2001, *ApJ*, 561, 22
- Klypin, A. & Prada, F. 2018, *MNRAS*, 478, 4602
- Klypin, A., Prada, F., Betancort-Rijo, J., & Albareti, F. D. 2018, *MNRAS*, 481, 4588
- Kofman, L., Bertschinger, E., Gelb, J. M., Nusser, A., & Dekel, A. 1994, *ApJ*, 420, 44
- Kofman, L., Pogosian, D., & Shandarin, S. 1990, *MNRAS*, 242, 200
- Kofman, L., Pogosyan, D., Shandarin, S. F., & Melott, A. L. 1992, *ApJ*, 393, 437
- Kofman, L. A. & Shandarin, S. F. 1988, *Nature*, 334, 129
- Lahav, O., Itoh, M., Inagaki, S., & Suto, Y. 1993, *ApJ*, 402, 387
- Lewis, A., Challinor, A., & Lasenby, A. 2000, *ApJ*, 538, 473
- Liivamägi, L. J., Tempel, E., & Saar, E. 2012, *A&A*, 539, A80
- Lokas, E. L., Juszkiewicz, R., Weinberg, D. H., & Bouchet, F. R. 1995, *MNRAS*, 274, 730
- Mandelbrot, B. B. 1982, *The Fractal Geometry of Nature*, ed. Mandelbrot, B. B.
- Mao, Q., Berlind, A. A., McBride, C. K., et al. 2014, *MNRAS*, 443, 1402
- Marinoni, C., Guzzo, L., Cappi, A., et al. 2008, *arXiv e-prints*, [arXiv:0811.2358](#)
- Marinoni, C., Le Fèvre, O., Meneux, B., et al. 2005, *A&A*, 442, 801
- Pandey, B., White, S. D. M., Springel, V., & Angulo, R. E. 2013, *MNRAS*, 435, 2968
- Peebles, P. J. E. 1980, *The large-scale structure of the universe* (Princeton Univ. Press)
- Pogosyan, D., Pichon, C., Gay, C., et al. 2009, *MNRAS*, 396, 635
- Press, W. H., Teukolsky, S. A., Vetterling, W. T., & Flannery, B. P. 1992, *Numerical recipes in FORTRAN. The art of scientific computing* (Cambridge University Press)
- Romeo, A. B., Agertz, O., Moore, B., & Stadel, J. 2008, *ApJ*, 686, 1
- Saar, E. 2009, in *Lecture Notes in Physics*, Berlin Springer Verlag, Vol. 665, *Data Analysis in Cosmology*, ed. V. J. Martínez, E. Saar, E. Martínez-González, & M.-J. Pons-Bordería, 523–563
- Shin, J., Kim, J., Pichon, C., Jeong, D., & Park, C. 2017, *ApJ*, 843, 73
- Smith, R. E., Peacock, J. A., Jenkins, A., et al. 2003, *MNRAS*, 341, 1311
- Springel, V. 2005, *MNRAS*, 364, 1105
- Starck, J.-L. & Murtagh, F. 2006, *Astronomical Image and Data Analysis*
- Szapudi, I. 2009, *Introduction to Higher Order Spatial Statistics in Cosmology*, ed. V. J. Martínez, E. Saar, E. Martínez-González, & M. J. Pons-Bordería, Vol. 665 (Springer), 457–492
- Takahashi, R., Sato, M., Nishimichi, T., Taruya, A., & Oguri, M. 2012, *ApJ*, 761, 152
- Tarenghi, M., Tifft, W. G., Chincarini, G., Rood, H. J., & Thompson, L. A. 1978, in *IAU Symposium, Vol. 79, Large Scale Structures in the Universe*, ed. M. S. Longair & J. Einasto, 263
- Tegmark, M., Strauss, M. A., Blanton, M. R., et al. 2004, *Phys. Rev. D*, 69, 103501
- Tully, R. B. & Fisher, J. R. 1978, in *IAU Symposium, Vol. 79, Large Scale Structures in the Universe*, ed. M. S. Longair & J. Einasto, 214
- Uhlemann, C., Codis, S., Hahn, O., Pichon, C., & Bernardeau, F. 2017, *MNRAS*, 469, 2481
- van de Weygaert, R., Shandarin, S., Saar, E., & Einasto, J., eds. 2016, *IAU Symposium, Vol. 308, The Zeldovich Universe: Genesis and Growth of the Cosmic Web*
- Zeldovich, Y. B. 1970, *A&A*, 5, 84
- Zeldovich, Y. B. 1978, in *IAU Symposium, Vol. 79, Large Scale Structures in the Universe*, ed. M. S. Longair & J. Einasto, 409–420
- Zeldovich, Y. B., Einasto, J., & Shandarin, S. F. 1982, *Nature*, 300, 407

Appendix A: Density estimates and power spectra

Appendix A.1: Kernel density estimates

One of the ways to calculate the density field is by a kernel sum (Davison & Hinkley 1997):

$$\rho(\mathbf{r}) = \sum_{i=1}^N K(\mathbf{r} - \mathbf{r}_i), \quad (\text{A.1})$$

where the sum is over all N data points, \mathbf{r}_i are the coordinates of data points, K is the kernel.

Kernels K are required to be distributions, positive everywhere and integrating to unity; in our case,

$$\int K(\mathbf{y}) d^3y = 1. \quad (\text{A.2})$$

Good kernels for smoothing densities to a grid are the box splines B_k . They are local and they are interpolating on a grid:

$$\sum_i B_k(x - i) = 1, \quad (\text{A.3})$$

for any x and a small number of indices that give non-zero values for $B_k(x)$. To create our density fields we use the popular B_3 spline function:

$$B_3(x) = \frac{|x-2|^3 - 4|x-1|^3 + 6|x|^3 - 4|x+1|^3 + |x+2|^3}{12}. \quad (\text{A.4})$$

This function differs from zero only in the interval $x \in (-2, 2)$, meaning that the sum in (A.3) only includes values of $B_3(x)$ at four consecutive arguments $x \in (-2, 2)$ that differ by 1. Figure A.1 shows the shape of the function in comparison to a Gaussian. One should note that in this formulation, implicitly, the smoothing scale and input particle coordinates are given in units of grid cell length and smoothing scale is equal to one.

If we choose B_3 to be our kernel function: $K_B^{(1)}(x) = B_3(x)$, then the three-dimensional kernel $K_B^{(3)}$ is given by a direct product of three one-dimensional kernels:

$$K_B^{(3)}(\mathbf{r}) \equiv K_B^{(1)}(x) K_B^{(1)}(y) K_B^{(1)}(z), \quad (\text{A.5})$$

where $\mathbf{r} \equiv \{x, y, z\}$. Although this is a direct product, it is isotropic to a very high degree (Saar 2009).

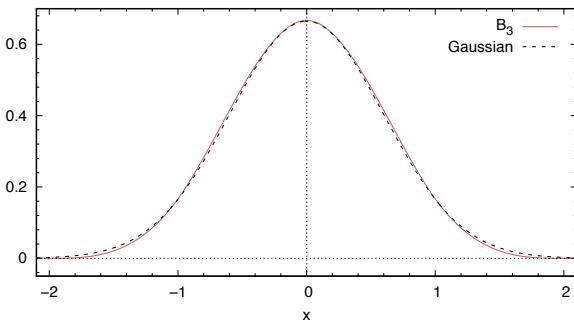


Fig. A.1. The shape of the box spline kernel B_3 . Solid line – the $B_3(x)$ kernel; dashed line – a Gaussian with $\sigma = 0.6$.

To increase the smoothing scale one can introduce a scale parameter to the kernel function K (together with the appropriate normalisation). However, in practice this also raises the number of particles in the kernel volume and the computation can quickly become uneconomical. One of the benefits of using the

B_3 smoothing kernel, is that one can employ the à trous wavelet algorithm and, having an existing density field as basis, calculate a field with twice the smoothing length by convolution with a simple discrete filter (Starck & Murtagh 2006).

$$C_{j+1}(i_x, i_y, i_z) = \sum_{l,m,n} H(l, m, n) C_j(i_x + 2^j l, i_y + 2^j m, i_z + 2^j n). \quad (\text{A.6})$$

Here C_j and C_{j+1} denote correspondingly the initial and smoothed density fields. Thus only the first density field needs to be calculated using particle coordinates. Convolution mask H is constructed as the following direct product

$$H = h \otimes h \otimes h, \quad (\text{A.7})$$

where the coefficients h are derived from the à trous discrete wavelet transform and its values corresponding to B_3 function are:

$$h = \left\{ \frac{1}{16}; \frac{1}{4}; \frac{3}{8}; \frac{1}{4}; \frac{1}{16} \right\}. \quad (\text{A.8})$$

Appendix A.2: Cubic-Cell density estimate

Smoothing lengths of original density fields from numerical simulation output have a resolution, equal to the size of the simulation cell, L_0/N_{grid} , this we call smoothing rank zero. We use a smoothing recipe, which increases the smoothing length by a factor of 2. We use this recipe successively 4 times, and get four smoothing ranks 1 to 4. For clarity we show in the core text smoothing length in units of h^{-1} Mpc.

In case of the cubic-cell smoothing we divided the original computational box of size L_0 with resolution $N_{\text{grid}} = 512$ to boxes of smaller resolution, $N_{\text{grid}} = 256, 128, 64, 32$, by counting densities in respective cells of the field in previous smoothing length. This yields smoothing lengths $R_l = L_0/N_{\text{grid}} h^{-1}$ Mpc. Smoothing lengths for rank 1 are $R_1 = L_0/256 h^{-1}$ Mpc, $R_2 = L_0/128 h^{-1}$ Mpc for rank 2, and so on. The main difference between smoothing rules is, that B_3 spline and top-hat rules preserve grid size, but the cubic-cell rule yields density fields with decreasing grid sizes N_{grid} .

Appendix A.3: Top-hat density and error estimates

Top-hat smoothed densities for L256, L512 and L1024 simulations were calculated at the nodes of a 512^3 regular cubic grid using smoothing radii for ranks 1 to 4, as explained in previous subsection.

The errors for the moments of the density distribution were determined via jackknife resampling: a full simulation box was divided into smaller cubes, each time omitting one of the small cubes while calculating the statistical moments. The variability of the calculated moments gives directly the desired error estimates (Efron 1982). We chose to split the simulation box into $2^3, 4^3$ and 8^3 equal-sized subcubes. The error estimates for all of these three choices did not vary significantly. In Figures with error we use the errors for the second choice, i.e. $4^3 = 64$ sub-volume case, only. We note that errors of all quantities (variance, K, S, S_3, S_4) were found separately.

PDFs of density fields and their moments can have systematic errors. We discuss these errors in the next Appendix.

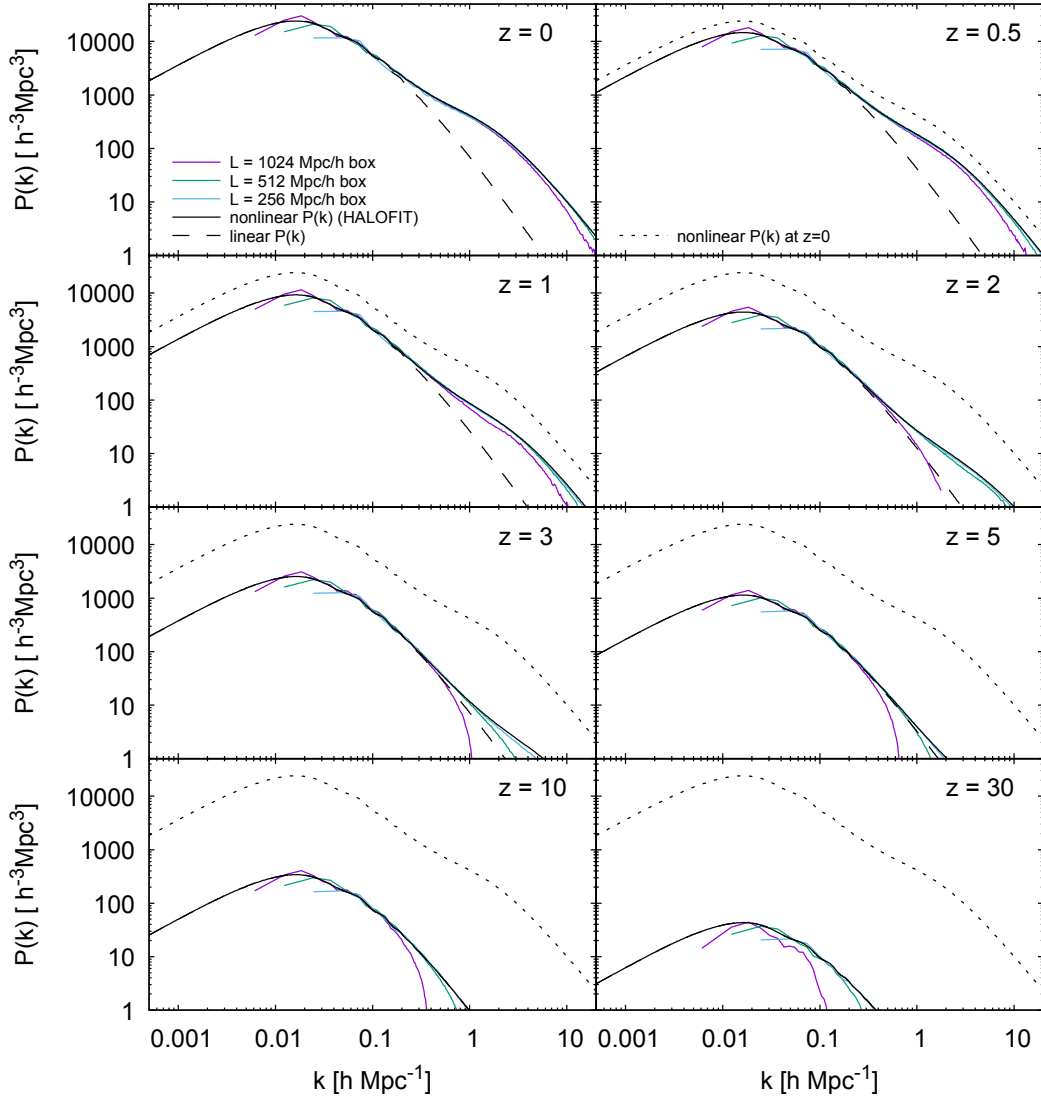


Fig. A.2. Comparison of simulation power spectra with the corresponding linear spectra and nonlinear HALOFIT results at various epochs z .

Appendix A.4: Evolution of the dark matter power spectra

Here we perform a simple consistency check for our GADGET simulations. In particular, we calculate the density power spectra for all the output redshifts and box sizes, resulting in total of $8 \times 3 = 24$ spectra. The spectra were calculated using FFTs on a 1024^3 regular cubic grid. The simulation particles were assigned to a grid via the triangular-shaped cloud (TSC) mass-assignment scheme. The shot-noise removal, grid smoothing and aliasing correction tailored for the TSC-scheme were applied, following the description given by Jing (2005).

The results of these calculations are shown in Figure A.2. Here the panels correspond to simulation snapshot redshifts displayed at the upper righthand corners, *i.e.*, they grow from left-to-right and from top-to-bottom directions. In comparison, with black solid lines, we show the nonlinear spectra according to the analytic HALOFIT approximation Smith et al. (2003); Takahashi et al. (2012) as implemented in the cosmological Boltzmann code package CAMB¹ Lewis et al. (2000). The corresponding linear spectra (also obtained via CAMB) are plotted with long dashed lines. As a reference, the dotted lines in all of the panels with $z > 0$ show the $z = 0$ nonlinear spectrum.

¹ <https://github.com/cmbant/CAMB>

One can see that the agreement between our simulation spectra and the well-tested analytic HALOFIT results is mostly very good. As expected, the bigger boxes perform better at larger scales, while their lack of resolution at smaller scales cannot properly account for the small-scale nonlinear evolution. In conjunction, except for the highest redshifts, the chosen three box sizes are reasonably good for capturing the dynamics of structure formation over more than three orders of magnitude in scale.

Appendix B: Comparison of moments obtained with different smoothing recipes

We performed smoothing of our GADGET simulations with three different kernels, the B_3 kernel, cubic-cell kernel and top-hat kernel. All kernels yields density fields, which are partly distorted due to non-sufficient resolution of our simulations for low-density regions. Our simulations contain one DM particle per computation cell. During the evolution the density in voids decreases, and there are less than one particle per cell. At the present epoch the mean density in central regions of voids is about one particle per ten cells. In calculation of the density field most cells in under-dense regions contain no particles and have zero density. This distorts smoothed density values in under-

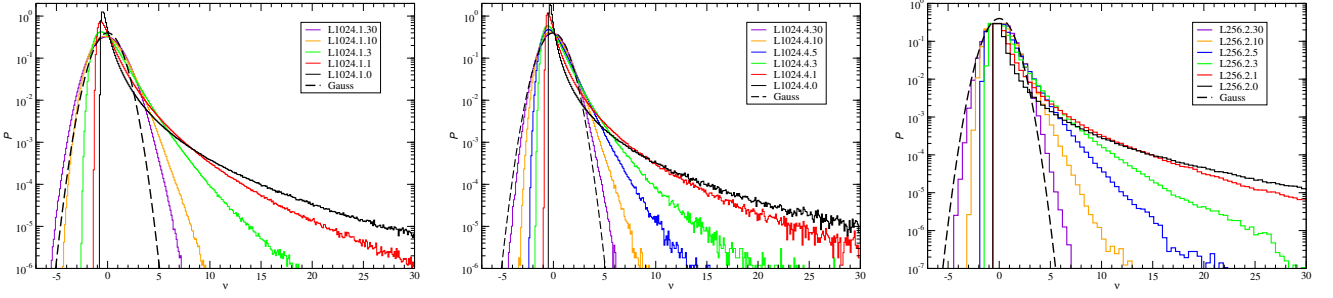


Fig. B.1. PDFs as functions of reduced densities $\nu = \delta/\sigma$, smoothed with different methods. *Left and central panels* show L1024.1 simulations, smoothed with B_3 spline and cubic-cell method, respectively, using smoothing kernel length $R = 4 h^{-1}$ Mpc. *Right panel* shows the L256.2 simulation, smoothed with the top-hat method with kernel $R = 2 h^{-1}$ Mpc. Smoothing rank is the first index in the simulation name, redshift is the second index. Colours indicate the evolutionary epoch $z = 30, 10, 5, 3, 1, 0$. Dashed bold lines show the Gaussian distribution.

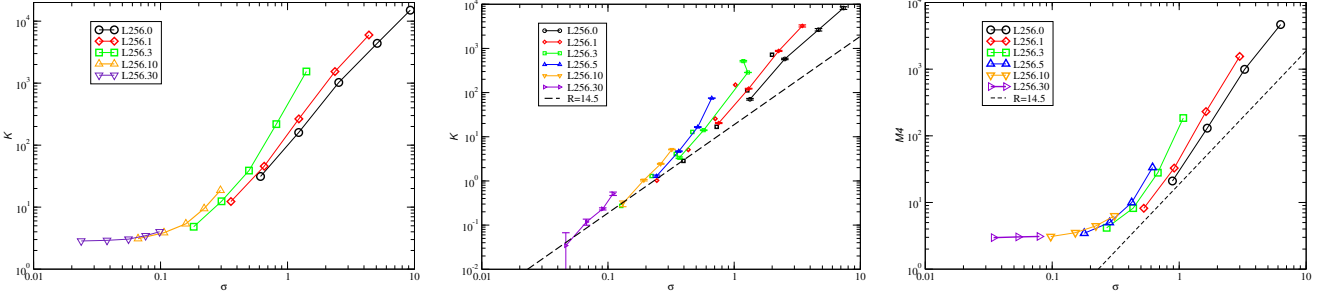


Fig. B.2. Mathematical kurtosis $K(\sigma)$ of the L256 simulation using various smoothing algorithms. *Left panel* shows results for smoothing with B_3 spline, *central panel* shows results with cubic-cell smoothing, *right panel* results for kurtosis, $M_4 = K + 3$ using top-hat smoothing. Name index shows redshift. Dashed bold lines show $K = 16\sigma^2$.

dense regions. For this reason we did not use original density fields of zero smoothing rank. But some problems exists also using higher smoothing ranks. In this section we discuss some results for different smoothing kernels.

In Figure B.1 we compare PDFs obtained with different smoothing recipes. In the left panel we show PDFs calculated with the B_3 spline for the L1024.1, smoothed with kernel of length $R_B = 4h^{-1}$ Mpc, for simulation epochs $z = 0, 1, 3, 10, 30$, given as the second index of the sample name. We see that PDF for simulation epochs $z = 10, 30$ are too wide, as compared with the Gaussian distribution.

The central panel of Figure B.1 shows PDFs of the simulation L1024.1, smoothed with the cubic-cell kernel of rank 1, which corresponds to smoothing length $R_B = 4h^{-1}$ Mpc. The right panel shows PDFs of the simulation L256.2, smoothed with with top-hat recipe using rank 2, which corresponds to $R = 2h^{-1}$ Mpc. The Figure shows that both top-hat smoothing recipes form PDFs with expected behaviour.

Figure B.2 shows the mathematical kurtosis K of the L256 simulation using various smoothing recipes. The left panel shows excess kurtosis of all three simulations smoothed with B_3 spline. Coloured lines show various simulation epochs, for each epoch symbols, starting from top, correspond to smoothing ranks 0 to 4. The Figure shows that for epochs $z = 10$ and 30 kurtosis does not approach to the expected value for a near Gaussian distribution $K \rightarrow 0$, but to a higher value, $K \rightarrow 2.8$. In other words, for these simulation epochs the PDF curve is leptokurtic, i.e. has heavy tails on both sides, as seen in the left panel of Figure B.1. Look for comparison the PDF of the same simulation calculated with both top-hat recipes, shown in the central and right panels of the Figure B.1.

Central panel of Figure B.2 shows the mathematical kurtosis K for the same L256 simulation, smoothed with the cubic-cell

method. As we see, over the whole σ interval the kurtosis K is proportional to σ^2 , as expected. The right panel of Figure B.2 shows the kurtosis $M_4 = K + 3$ for the top-hat smoothing for L256 simulation. It is expected that at low $\sigma \rightarrow 0$ this function approaches $K(\sigma) + 3 \rightarrow 3$. The Figure shows that actually $K(\sigma) + 3 \rightarrow 2.9$. This means that at low σ some vales of K are negative. These deviations are larger than deviations, expected from random errors, shown in Figure 7. In other words, here we have small, but systematic errors.

For simulations at epoch $z = 30$ and smoothing with the cubic-cell kernel of rank 4 we obtained for S_4 slightly negative values. This is not surprising, since densities at this redshift are close to the mean density, S_4 is found by subtraction of two approximate equal numbers, and the expected values of the kurtosis are smaller than estimated errors. In these cases we accepted for the cosmological kurtosis at $z = 30$ the value on the basis of lower redshift, $S_4 = 16$, and calculated mathematical kurtosis K using Eq. (11).

Appendix C: Analytical approximations for the evolution of skewness and kurtosis

We fit results of the evolution of $S_3(\sigma)$ and $S_4(\sigma)$ using a 4-parameter functional form. If S is either S_3 or S_4 , then the approximation can be written as:

$$S = S_{\min} + \frac{C_1 \sigma^{5/2}}{1 + C_2 \sigma^{5/2}}, \quad (\text{C.1})$$

where S_{\min} is the minimum value of S , and parameters C_1 and C_2 describe the shape of the function $S(\sigma)$. Specifically, the ratio C_1/C_2 gives the magnitude of the total increase of S :

$$C_1/C_2 = S_{\max} - S_{\min}. \quad (\text{C.2})$$

Another shape parameter is S_1 , which is the value of S at $\sigma = 1$. Using parameters S_{\min} , S_1 , and S_{\max} we can find C_1 and C_2 :

$$C_1 = \frac{(S_1 - S_{\min})(S_{\max} - S_{\min})}{(S_{\max} - S_1)}, \quad C_2 = \frac{C_1}{(S_{\max} - S_{\min})}. \quad (\text{C.3})$$

The evolution of S is described by a power-law dependence of S_1 and S_{\max} on the redshift z :

$$S_1 = S_{10}(1+z)^\alpha, \quad S_{\max} = S_{\max,0}(1+z)^\alpha, \quad (\text{C.4})$$

where α is a free parameter describing the evolution with time. Here S_{10} and $S_{\max,0}$ are shape parameters estimated at $z = 0$.

This approximation has 4 free parameters: three shape parameters S_{\min} , S_{10} , and $S_{\max,0}$ and parameter α that describes the evolution. Having these parameters one finds C_1 and C_2 using Eq.(C.3). Now we can use Eq.(C.1) to estimate parameters S_3 and S_4 . For cosmology used for GLAM simulations and for reduced skewness S_3 the parameters are: $S_{3,\min} = 3.5$, $S_{3,10} = 4.9$, and $S_{3\max,0} = 9.4$. Parameter α depends on redshift. We find that for $z \lesssim 1.5$ the parameter is $\alpha = 0.25$. For larger redshifts the evolution is slightly faster: $\alpha = 0.43$. These approximations give 5 per cent accuracy for S_3 . This fit was tested and can only be used for $z \lesssim 20$ and for $\sigma > 0.05$.